ATMOSPHERIC ENVIRONMENT: X 27 (2025) 100361

Contents lists available at ScienceDirect

Atmospheric Environment: X

journal homepage: www.journals.elsevier.com/atmospheric-environment-x

Unraveling the global response of secondary atmospheric pollutants to emission reductions imposed during the COVID-19 pandemic

Apostolos T. Koumparos [a], Vlassis A. Karydis [a], Georgios I. Gkatzelis [a], Nikolaos Mihalopoulos [b], Alexandra P. Tsimpidi [a,*]

[a] Institute of Climate and Energy Systems: Troposphere (ICE-3), Forschungszentrum Jülich GmbH, Jülich, Germany
[b] National Observatory of Athens, Inst. for Environment Res. & Sustainable Dev., Athens, 15236, Greece

ARTICLE INFO

Keywords:
COVID-19 emission reductions
Air quality changes
Secondary atmospheric pollutants
Ozone and $PM_{2.5}$ dynamics
Sectoral and spatial pollutant trends
Chemistry-climate modeling

ABSTRACT

This study employs the global chemistry–climate model EMAC, combined with emission adjustment factors (CONFORM), to evaluate the global impacts of the 2020 COVID-19 lockdowns on secondary air pollutants. Unlike earlier studies limited to short periods or specific regions, this work captures seasonal, spatial, and sectoral variability in emissions and pollutant formation. It examines both primary pollutants (e.g., NO_x, SO_2) and secondary pollutants such as ozone and $PM_{2.5}$ components. Significant NO_x reductions were simulated, with peak decreases of 31 % in Europe and 25 % in Eastern Asia during lockdowns. SO_2 dropped by up to 20 % in Southern Asia, while Eastern Asia saw a 14 % post-lockdown rebound due to increased industrial activity. Ozone responses varied regionally, with increases of up to 4 % in urban areas in Eastern Asia due to reduced titration, while Southern Asia saw decreases up to 1.4 %. Aerosol concentrations followed similar regional trends. Sulfate declined by 17 % in Southern Asia while nitrate and ammonium dropped by 27 % and 33 % in Europe, respectively. Global primary organic aerosol decreased by 4 %, with South Asia showing an 8 % reduction. Secondary organic aerosol fell by 4 %, with the largest drop (8 %) in Latin America and the Caribbean. Overall, $PM_{2.5}$ over land declined by 2 %, with Europe showing the largest regional decrease (6 %). These results highlight the substantial but regionally varied effects of pandemic-related emission changes. However, even substantial short-term reductions had limited impact on $PM_{2.5}$ levels, underscoring the need for sustained, large-scale emission cuts to meet WHO air quality guidelines.

1. Introduction

The COVID-19 pandemic led to unprecedented restrictions on human activities, especially travel and commuting, resulting in rapid reductions in anthropogenic pollutant emissions. Most countries imposed social distancing measures, which affected not only the transportation sector but also many businesses, which were temporarily out of operation, while industry and manufacturing sectors had the minimum workload (Skiriene and Stasiskiene, 2021). In contrast, residential activity and the use of biomass and coal for heating and cooking increased (Kong et al., 2023; Tian et al., 2021). Restrictions in the transport sector during the shutdowns affected NO_x emissions (Guevara et al., 2022), while changes in the power and industrial sectors mainly affected SO_2 emissions (Amritha et al., 2024). Therefore, the impacts on air quality may differ between urban and suburban areas (Wang et al., 2021). These global changes provide an opportunity to study how atmospheric composition responds to these pandemic-driven changes in emissions, and to examine their impact on the formation of secondary air pollutants such as ozone (O_3) and fine particulate matter ($PM_{2.5}$).

Several studies have examined the influence of COVID-19 lockdowns on air pollutant emissions and air quality in North America (Goldberg et al., 2020; Jia et al., 2020; Forster et al., 2020), Europe (Petetin et al., 2020; Ropkins and Tate, 2021; Cameletti, 1994; Giani et al., 2020), and Asia (Zheng et al., 2020; Weber et al., 2020; Tian et al., 2021; Kong et al., 2023; Ren et al., 2021; Kang et al., 2021; Li et al., 2022; Le et al., 2020; Gao et al., 2021; Wang et al., 2021). Global-scale assessments have also conducted (Doumbia et al., 2021; Gaubert et al., 2021; Gkatzelis et al., 2021b; Yang et al., 2020; Fu et al., 2020; Smith et al., 2022; Adam et al., 2021; Sanap, 1994; Cao et al., 2021; Tang et al., 2021), many of which report a global drop in CO_2 emissions of about 6 %, and decreases in NO_x emissions ranging from 11 % to 29 % (Guevara et al., 2022; Camargo-Caicedo et al., 2021; Wang et al., 2024). Forster et al. (2020) and

* Corresponding author.
E-mail address: a.tsimpidi@fz-juelich.de (A.P. Tsimpidi).

https://doi.org/10.1016/j.aeaoa.2025.100361
Received 16 April 2025; Received in revised form 30 June 2025; Accepted 25 August 2025
Available online 26 August 2025

Hanaoka and Masui (2020) reported a 30 % decline in global NO_x emissions in April 2020. Meanwhile, Amritha et al. (2024) reported a global average SO_2 reduction of 2 %, based on satellite observations. These studies confirm widespread changes in atmospheric composition due to reduced transportation and industrial activity, with strong regional variability. Satellite-based retrievals further support these trends, showing declines in tropospheric NO_2 and SO_2 columns over key regions. Sekiya et al. (2023) found reductions of 19–25 % for NO_2 and 14–20 % for SO_2 over North America, Europe, and East Asia in April 2020. Local studies in China and India also indicated drops of up to 40 % in NO_2 concentrations (Zheng et al., 2020; Xia et al., 2021). However, such declines were often short-lived, with emissions increasing again within a few months (Liu et al., 2020; Dong et al., 2022).

A large number of studies have also investigated the influence on atmospheric aerosol concentrations (Rodriguez-Urrego and Rodriguez-Urrego, 2020; Sekiya et al., 2023; Gkatzelis et al., 2021b; Hammer et al., 2021; Venter et al., 2020; Fu et al., 2020; Zheng et al., 2021; Tian et al., 2021; Le et al., 2020; Sanap, 1994; Liu et al., 2021a; Collivignarelli et al., 2020; Stratoulias and Nuthammachot, 2020). Global $PM_{2.5}$ levels fell by approximately 31 % during the lockdowns (Venter et al., 2020), while PM_{10} decreased by 8–40 % depending on location (Gkatzelis et al., 2021b). Regionally, China and India saw substantial $PM_{2.5}$ reductions of 24 % and up to 37 %, respectively (Zheng et al., 2021; Kant et al., 2020). Satellite data confirmed sulfate and nitrate aerosol reductions of 8–21 % in polluted regions (Sekiya et al., 2023), though in some areas, such as Rome, $PM_{2.5}$ increased due to sustained local emissions (Fu et al., 2020). Wildfires also contributed to elevated aerosol levels in South America, Mexico, and parts of Africa (Sanap, 1994).

Ozone responses were more complex. A significant number of studies have investigated the effects of COVID-19 lockdowns on O_3 (Gkatzelis et al., 2021b; Le et al., 2020; Fu et al., 2020; Liu et al., 2021a; Venter et al., 2020; Adam et al., 2021; Gao et al., 2021; Patel et al., 2020; Collivignarelli et al., 2020; Lian et al., 2020; Sharma et al., 2020; Sicard et al., 2020). While NO_x reductions in NO_x-saturated urban areas led to reduced O_3 titration and consequent increases in O_3 up to 14 ppb (Le et al., 2020; Tang et al., 2021), some NO_x-limited regions experienced modest decreases in O_3 levels. Liu et al. (2021a) found that global O_3 Air Quality Index (AQI) rose by 10–27 % across many cities, while Venter et al. (2020) observed a 4 % average increase in 34 countries. These shifts were closely tied to VOC/NO_x sensitivity and seasonal photochemical regimes, with implications for secondary aerosol formation (Adam et al., 2021).

Finally, a range of chemical transport and chemistry–climate models have simulated the atmospheric effects of the COVID-19 lockdowns. Giani et al. (2020), using WRF-Chem, found a 30 % reduction in $PM_{2.5}$ over China and a 17 % reduction over Europe in early 2020. Gaubert et al. (2021), employing CESM, observed wintertime increases in ozone across northern China, Europe, and the United States, even amid NO_x and VOC reductions, while O_3 decreased in rural NO_x-limited regions. Additional studies using the CAM-chem model, including Ortega et al. (2023), reported a mean decline of 9 % ± 5 % in tropospheric column O_3 between March and May 2020, based on observational sites worldwide. Similarly, Bouarar et al. (2021), using the CAM-chem model, found that free tropospheric O_3 during spring and summer was 5–15 % lower than climatological norms, while in the Southern Hemisphere, COVID-19-related O_3 decreases of 4–6 % were offset by simultaneous O_3 increases from other atmospheric influences. Other regional-scale studies using models such as WRF, CHIMERE, COSMO-ART, and HYSPLIT (e.g., Le et al., 2020; Huang et al., 2021; Casallas et al., 2024) also captured region-specific patterns in air quality changes. These results emphasize that model outcomes are highly sensitive to the choice of emission inventories, chemistry schemes, meteorological inputs, and resolution, all of which contribute to variability in simulated air quality responses.

While most studies have focused on the first six months of 2020 to assess the impact of COVID-19 lockdowns on air quality, a comprehensive year analysis is crucial to fully understand the long-term effects. Many existing studies have also been limited to specific regions or periods, often overlooking the seasonal, sectoral, and spatial emission variations and their impact on secondary pollutants. To address this gap, the present study employs a global modeling approach that covers the entire year of 2020, allowing for a complete evaluation of the pandemic's effects on global air quality and capturing the nuanced changes in emissions and pollutant formation across different regions and seasons. Between 2019 and 2020, the changes in emissions in residential combustion, public energy, industry, and shipping sectors were also influenced by factors unrelated to COVID-19, such as meteorological changes (in particular a warmer winter) (Guevara et al., 2022). In this work, the ECHAM5/MESSy Atmospheric Chemistry (EMAC) model is used for the first time to quantify the impact of national lockdowns for the control of COVID-19 on regional and global air quality during the year 2020, focusing on both primary and secondary pollutants. The Copernicus Atmosphere Monitoring Service (CAMS) emission inventory has been modified based on the gridded adjustment factors of the CONFORM (COvid-19 adjustmeNt Factors fOR eMissions) dataset (Doumbia et al., 2021). These adjustment factors vary temporarily and are source specific (i.e., transportation, power generation, industry, and residential) to account for changes in emissions imposed by each country during the pandemic. This modeling framework allows us to isolate and evaluate the atmospheric impacts of lockdown-related emission changes with high spatial and temporal resolution, offering insights relevant for both evaluating short-term effects on air quality but also for assessing long-term strategies aimed at reducing pollution and mitigating climate change.

2. Emissions description

2.1. Emissions inventory

In the current study, the Copernicus Atmosphere Monitoring Service (CAMS v4.2) anthropogenic emissions inventory was used to simulate a business-as-usual scenario (BAU) if no lockdowns enforced during the year 2020. CAMS includes 36 chemical species emitted by 20 sectors (Granier et al., 2019) with a monthly temporal coverage and a global spatial coverage of $0.1 \times 0.1^{\circ}$ grid resolution. The global emission fluxes provided by CAMS for the year 2020 are 71.7 Tg yr^{-1} NO_x, 66.7 Tg yr^{-1} NH_3, 98.3 Tg yr^{-1} SO_2, 4.7 Tg yr^{-1} BC, and 11.7 Tg yr^{-1} OC. ˙. Emissions from open biomass burning were obtained from the GFEDv3.1 database (Van Der Werf et al., 2010). Organic compound (OC) emissions released by the combustion of fossil fuels, biofuels, and biomass burning (i.e., in savannah and forest fires) are introduced in the model as low volatility (LVOC; $C^* < 0.32$ μg m^{-3}), semivolatile (SVOC; 0.32 μg m^{-3} $< C^* <$ 320 μg m^{-3}), and intermediate volatility (IVOC; 320 μg m^{-3} $< C^* < 3.2 \times 10^6$ μg m^{-3}) organic compounds by using the emission factors of Tsimpidi et al. (2016).

Sea salt mineral dust, and volcanic SO_2 emissions are based on the AEROCOM dataset (Dentener et al., 2006). Sea salt consists of 30.6 % Na^+, 3.7 % Mg^{2+}, 1.2 % Ca^{2+}, 1.1 % K^+ and 55 % Cl. Mineral cations such as Ca^{2+}, Mg^{2+}, K^+, and Na^+ are considered as the chemically active components of the emitted bulk dust (Karydis et al., 2016; Klingmuller et al., 2018). Biogenic emissions of NO from soils are calculated online (Yienger and Levy, 1995) while NO_x from lighting is also calculated online (Grewe et al., 2001). Emissions of oceanic dimethyl sulfide (DMS) are calculated online by the AIRSEA submodel (Pozzer et al., 2006). The GEIA data set has been used to provide oceanic ammonia emissions and emissions from soils under natural vegetation (Bouwman et al., 1997).

2.2. Emissions Adjustment factors

To simulate the impact of reduced atmospheric emissions on regional and global air quality during the COVID-19 pandemic, the CONFORM

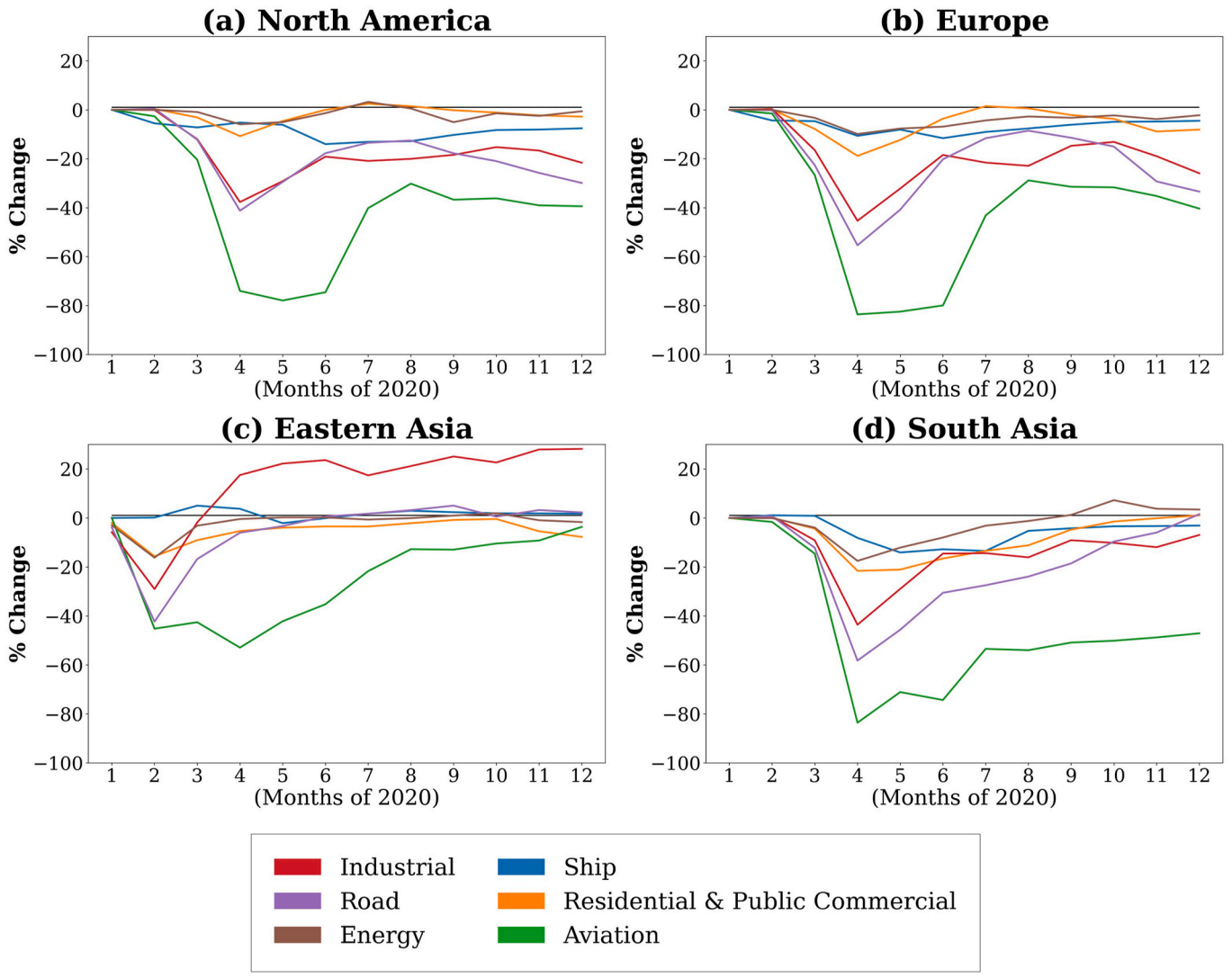

Fig. 1. Monthly average adjustment factors used to estimate emission changes during the COVID-19 pandemic in the regions of **(a)** North America, **(b)** Europe, **(c)** Eastern Asia, and **(d)** South Asia. The sectors affected include Shipping, Residential and Public Commercial, Industry, Road Transport, and Energy.

adjustment factors (Doumbia et al., 2021) were applied to the CAMS v4.2 anthropogenic emissions inventory. The CONFORM dataset provides gridded adjustment factors for the transportation, power generation, industry, ships, and residential public and commercial sectors at the same spatial and temporal resolution as the CAMS v4.2 global anthropogenic emission inventory, on a daily, monthly, and annual basis, starting in January 2020. The averaged adjustment factors we used in our simulations are derived based on activity data from each country and continent, i.e., mobility trends and traffic congestion index for road transportation, container ship port calls for shipping, air traffic data for aviation, coal consumption and crude steel production for industry, total electricity load for power generation, and mobility trends for residential and commercial sectors (Doumbia et al., 2021).

To determine the influence of each most affected sector based on the CONFORM dataset for NO_x, SO_2, BC, OC, CO and anthropogenic VOCs (aVOCs) emissions, we calculated the global average emission share of each of the 6 pollutants from each sector. NO_x is mainly emitted by the energy (32 %), transportation (27 %), and industry (22 %) sectors, while SO_2 is mainly emitted by energy (43 %) and industry (40 %). Both BC and CO are mainly emitted by industry (38 % and 25 %, respectively) and the residential/commercial sector (~40 % for both). For OC, the residential/commercial sector is the main emitter (74 %). In the case of aVOCs, the industry and transportation sectors are the main emitters (~40 % for both). Considering these percentages, it is obvious that a small change in sectors such as industry and energy can significantly affect the emissions of certain air pollutants.

Fig. 1 depicts the timeseries of the adjustment factors for the year 2020, expressed as a percentage change in emissions from each sector following Doumbia et al. (2021). The results in Fig. S1 include the highly populated and industrialized regions of Eastern Asia, Europe, North America, and South Asia, where activity data are more accurate and largely available compared to other continents. During each COVID-19 lockdown (in February for Eastern Asia and in April for the remaining areas), the industrial and road transportation sectors were the most affected, in some cases with reductions of 40–55 % (Fig. S1 and S2). In contrast, the other sectors experienced a maximum reduction of around 10 %, especially in the first six months of 2020. On the other hand, in the case of Eastern Asia, the industry sector seems to have experienced a significant increase after April, in some cases reaching values of more than +20 %. The road transportation and shipping sectors in Eastern Asia show a slight increase in some cases after the month of July, with the shipping sector also showing an increase between February and April (Fig. 1 and S1). The energy and industry sectors also show increased emissions in Latin America in the second half of 2020 (Fig. S1 and S2). For South Asia, the energy sector increases in November (Fig. S1). Finally, the impact of global travel restrictions on the aviation

sector is evident worldwide, with most regions experiencing an average annual reduction of around 50 % (Fig. S1). In February, aviation was drastically reduced in the Eastern Asia region (Fig. 1 and S1) due to the first outbreak of the coronavirus, while in April regions such as North America and Europe began to impose travel restrictions and emissions from aviation were reduced by more than 80 %. After the spring months, the reduction slowed as coronavirus quarantine measures began to be relaxed.

2.3. Changes in pollutant emissions during the COVID-19 pandemic

Fig. 2 shows the monthly average percentage change (%) in emissions of the major pollutants between the COVID-19 pandemic and BAU scenarios for the regions of Eastern Asia, Europe, South Asia, and North America. Table 1 shows the corresponding annual average emissions changes for ten regions of the world considered. In Eastern Asia, emissions of all pollutants were reduced by more than 20 % in February, especially aVOCs (about 25 %; Fig. 2c) and NO_x (about 20 %; Fig. 2c) due to quarantine enforcement and drastic reductions in road traffic. However, after April, emissions increased sharply, leading to increases of up to 10 % compared to the BAU scenario, especially for SO_2, due to the increased activity of the industrial sector (Fig. 1). Overall, annual average pollutant emissions have increased compared to the BAU scenario, with the largest increase for aVOCs (5.4 %) and the smallest for NO_x (0.2 %). The largest decrease was for CO (1.6 %) followed by OC (1.4 %) as shown in Fig. 2c. These findings are in accordance with previous results reported by Liu et al. (2021b), Xia et al. (2021), and Zheng et al. (2021), which observed significant reductions in SO_2 and CO emissions in China during quarantine, followed by a rebound in pollutant emissions due to increased industrial activity and energy use, as highlighted by Dong et al. (2022). In contrast, pollutant emissions over Europe, North America, and South Asia decrease after March, with the largest reductions occurring in April (about 30 %; Fig. 2). Over South Asia, pollutant emissions gradually increase after April until they reach BAU levels in December (Fig. 2d). Over Europe (Fig. 2b) and North America (Fig. 2a), pollutant emissions start to increase after April reaching a minimum of about 10 % reductions compared to BAU levels during the summer months, after which they decrease again following the second wave of the coronavirus and the new closures. This inter-annual variation in pollutant emissions has been reported by other studies, showing similar seasonal trends influenced by pandemic restrictions and subsequent relaxations (Guevara et al., 2022).

North America shows the highest annual average reductions for aVOCs and CO (~12 % on average) driven by 20–40 % reductions in

Table 1
Percentage annual difference (%) of pollutant emissions between COVID-19 and BAU scenario. A negative result indicates a decrease during the corona period.

	NOx	aVOCs	BC	CO	SO_2	OC
North America	−8.0	−13.2	−9.3	−11.8	−9.5	−8.4
Europe	−12.5	−9.5	−11.4	−8.2	−8.2	−7.2
Eastern Asia	0.2	5.4	1.7	−1.6	2.7	−1.4
Southern Asia	−10.3	−10.9	−9.6	−10.0	−7.5	−6.5
Eurasia	−5.2	−9.5	−7.3	−6.4	−7.8	−6.0
South-East Asia and Developing Pacific	−7.8	−7.0	−5.7	−7.3	−6.4	−2.4
Asia-Pacific Developed	−11.5	−13.2	−12.6	−10.9	−8.6	−9.0
Middle East	−13.1	−13.7	−13.8	−13.9	−6.0	−12.9
Africa	−5.0	−5.0	−3.9	−3.6	−3.3	−2.6
Latin America & Caribbean	−16.9	−22.4	−15.8	−17.8	−9.0	−8.8

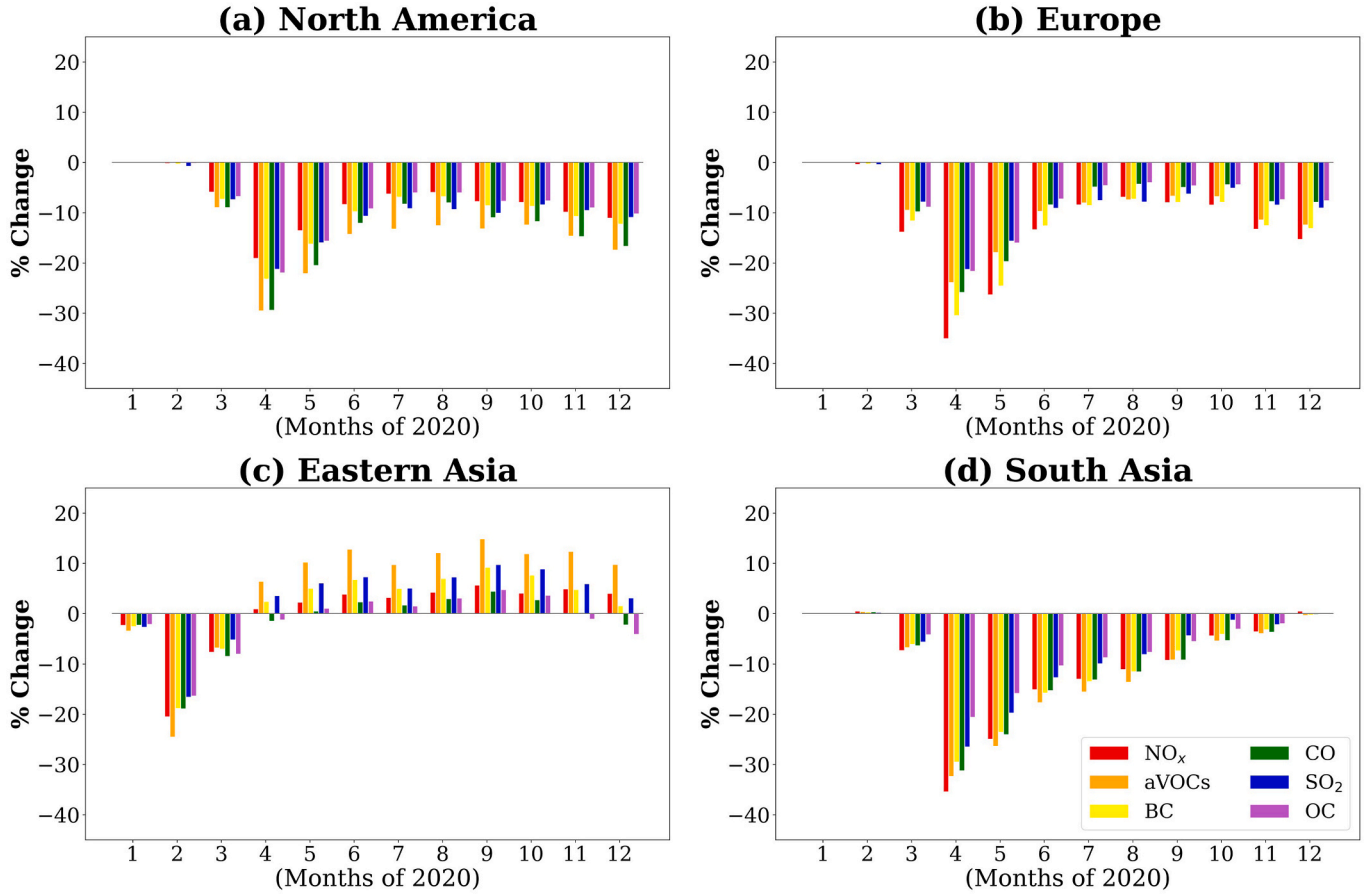

Fig. 2. Percentage change in NO_x, VOC, BC, CO, SO_2, and OC emissions after applying the COVID-19 adjustment factors in the CAMS v4.2 global anthropogenic emissions inventory over the areas of North America, Europe, Eastern Asia, and South Asia in 2020.

emissions from the industrial sector (Fig. 1 and S2). This aligns with reported CO declines of 5–10 % during the lockdown period (April to May 2020) compared to pre-lockdown levels (March 2020) in regions with significant human activity, including North America (Pathak et al., 2023). On the other hand, in Europe NO_x emissions are the most affected with annual average reductions of 12.5 % due to large reductions in transport emissions. Among the other regions, the largest reductions in pollutant emissions were observed in Latin America and the Caribbean, where aVOCs decreased by 22 % on annual average, while other pollutants decreased by 9 % (OC and SO_2; Table 1) to ~17 % (NO_x and CO; Table 1), as significant reductions in these pollutants were observed in large cities such as Buenos Aires, Lima, Rio de Janeiro, Sao Paolo, Mexico City, and Bogota (Poullain et al., 2022; Kutralam-Muniasamy et al., 2021; Pardo Amaya and Samuel, 2022; Rodriguez-Urrego and Rodriguez-Urrego, 2020) (Table 1). In the Middle East, most pollutants decreased by about 13 % except for SO_2 (6 %; Table 1), which is consistent with the reduction of 4 % reported by Amritha et al. (2024). In the Asia-Pacific developed region, pollutant emissions decreased by 9–13 %, while in the remaining regions (i.e., Africa, Eurasia, and Southeast Asia and developing Pacific), the annual average pollutant emission reductions are less than 10 % (Table 1) with the lowest reductions occurring in Africa.

3. Model description

3.1. Atmospheric chemistry model

In this study, the ECHAM5/MESSy Atmospheric Chemistry model (EMAC) is used, which is a global chemistry-climate model that describes lower and middle atmosphere processes and their interaction with oceans, land, and human influences (Jöckel et al., 2005). The European Center Hamburg (ECHAM5) general circulation model (Roeckner et al., 2006) is used as the atmospheric dynamical core to describe the atmospheric flow. The Modular Earth Submodel System (MESSy2) links the core model with sub-models that simulate gas-phase chemistry (MECCA; Sanap, 1994), inorganic aerosol microphysics (GMXe; Pringle et al., 2010), organic aerosol formation and growth (ORACLE; Tsimpidi et al., 2014), aerosol optical properties (AEROPT; Lauer et al., 2007), cloud microphysics (CLOUD; Jöckel et al., 2005), dry deposition and sedimentation (DRYDEP, SEDI; Kerkweg et al., 2006), and cloud scavenging (SCAV; Tost et al., 2006). In this study, we employed the EMAC model at a T63L31 resolution, corresponding to a horizontal grid spacing of approximately 1.875° × 1.875° and 31 vertical levels extending up to 10 hPa (~30 km altitude). The analysis presented here focuses on the surface level, which in the model corresponds to a layer extending up to approximately 67 m above ground level. EMAC is applied for 2 years, covering the period 2019–2020 in the lower troposphere, with 2019 used solely as the spin-up period. The model simulations are nudged towards meteorology using ERA5 data (Hersbach et al., 2020), ensuring meteorological consistency across both scenarios and isolating the impact of emission changes.

3.2. Organic aerosol formation

The ORACLE module (Tsimpidi et al., 2014, 2024) is employed to simulate the organic aerosol composition and evolution in the atmosphere based on the volatility basis set framework (VBS). It calculates the contribution of low volatility (LVOCs), semivolatile (SVOCs), intermediate volatility (IVOCs), and volatile organic compounds (VOCs) to the formation of POA and SOA by considering their gas-phase photochemical reactions that change their volatility and assuming bulk equilibrium between the gas and particulate phases. Rather than tracking individual compounds, ORACLE groups organics into volatility bins defined by their effective saturation concentration (C*). LVOCs ($C^* < 0.32$ μg/m^3) are extremely low-volatility compounds such as large multifunctional oxidation products. SVOCs ($0.32 < C^* < 320$ μg/m^3) include compounds like long-chain alkanes and oxygenated aromatics. IVOCs ($320 < C^* < 3.2 \times 10^6$ μg/m^3) typically include branched alkanes, cycloalkanes, and polycyclic aromatics. VOCs ($C^* > 0.32 \times 10^6$ μg/m^3) are represented by isoprene, terpenes, sesquiterpenes, as well as medium-chain alkanes, olefins, and aromatics.

POA are formed from the phase partitioning of LVOC and SVOC emissions from open biomass burning and fuel combustion sources. Gas-phase photochemical reactions that modify the volatility of the organics are considered, and the oxidation products of each group of precursors (SVOCs, IVOCs, and VOCs) can partition to the aerosol phase by assuming bulk equilibrium forming SOA. The volatilities of SVOCs and IVOCs are reduced by a factor of 10^2 because of the OH reaction with a rate constant of $2x10^{-11}$ cm^3 molec^{-1} s^{-1} and a 15 % increase in mass to account for two added oxygen atoms (Tsimpidi et al., 2018). LVOCs are not allowed to participate in photochemical reactions since they are already in the lowest volatility category. The VOC oxidation results in products distributed in four volatility categories with effective saturation concentrations of 10°, 10^1, 10^2, and 10^3 μg m^{-3}. These products are categorized as (i) anthropogenic and (ii) biogenic SOA. More details about the ORACLE module and the different aerosol types and chemical processes simulated by ORACLE in this study can be found in Tsimpidi et al. (2016).

3.3. Inorganic aerosol thermodynamics

The GMXe submodel simulates both the thermodynamic behavior of inorganic aerosols and their microphysical evolution, as described by Pringle et al. (2010). It is based on an enhanced version of the M7 aerosol scheme (Vignati et al., 2004), which represents aerosols using seven interacting lognormal modes, four hydrophilic and three hydrophobic. Within each mode, aerosols are assumed to be internally mixed (i.e., of uniform composition), but differences in composition are allowed between modes. The hydrophilic modes span the full-size range of atmospheric particles, covering nucleation, Aitken, accumulation, and coarse modes, while the hydrophobic modes represent similar size classes excluding nucleation. Each aerosol mode is characterized by its number concentration, mean particle radius, and geometric standard deviation. While the size boundaries of the modes are fixed, their mean radius can vary (Pringle et al., 2010).

The gas–aerosol partitioning of inorganic compounds is calculated using the ISORROPIA-II thermodynamic model (Fountoukis and Nenes, 2007), which accounts for the equilibrium between gas, aerosol, and solid phases. Aerosols may exist in either a stable state, where salts precipitate upon saturation, or a metastable state in which aerosols are always aqueous, and salt precipitation is not considered. While the two assumptions can lead to differences under low relative humidity, global-scale comparisons have shown minimal discrepancies across aerosol components (Karydis et al., 2021; Milousis et al., 2024). This study adopts the stable state configuration. To capture potential kinetic limitations in condensation, gas–aerosol partitioning is resolved in two steps. First, the uptake of condensable gases is estimated under the assumption of diffusion-limited condensation (Vignati et al., 2004). Then, ISORROPIA-II adjusts the gas–aerosol distribution assuming instantaneous thermodynamic equilibrium (Karydis et al., 2016).

3.4. Model evaluation

The EMAC model is widely used and recognized in the literature for its ability to accurately reproduce various atmospheric parameters, including organic and inorganic aerosol concentrations and compositions, gas-phase mixing ratios, aerosol optical depth, acid deposition, cloud properties, and meteorological parameters (Tsimpidi et al., 2017; Karydis et al., 2017; Pozzer et al., 2022; Milousis et al., 2025a). A comparison of the model's performance in estimating surface mass concentrations of $PM_{2.5}$ aerosol components is provided in the supplemental material (Fig. S7–S10 and Table S1). This comparison utilizes

observations from several monitoring networks across the Northern Hemisphere, including East Asia (EANET, The Acid Deposition Monitoring Network in East Asia), Europe (EMEP, European Monitoring and Evaluation Programme), and the USA, covering both urban (EPA-CSN, U.S. Environmental Protection Agency Chemical Speciation Network) and rural (IMPROVE, Interagency Monitoring of Protected Visual Environments) locations. IMPROVE primarily consists of rural background stations located in national parks and remote areas across the United States, aimed at tracking regional haze and visibility trends (Guevara et al., 2022). In contrast, EPA focuses on urban sites, capturing aerosol characteristics in more densely populated and industrialized areas (Lin et al., 2014). In Europe, EMEP stations include both urban and rural sites, though the majority used for model evaluation are in rural or suburban regions (Lu et al., 2024). EANET sites are predominantly rural, located in less industrialized areas across East and Southeast Asia to monitor regional background air quality and acid deposition trends (Zhang et al., 2020).

Sulfate aerosol concentrations are simulated with reasonable accuracy (Fig. S7, Table S1). The model underestimates sulfate in East Asia (NMB = −41 % at EANET), Europe (−20 % at EMEP), and urban North America (−28 % at EPA), but it overestimates in the rural North America (NMB = 94 % at IMPROVE). Nitrate aerosol is significantly overestimated, particularly in rural locations (Fig. S8, Table S1). At IMPROVE sites, the model yields an NMB of +502 %, while the overestimation is more moderate at EPA (+11 %) and EANET (+61 %). This bias likely reflects both known measurement uncertainties, such as volatilization losses of NH_4NO_3 from filters, and model limitations, including coarse grid resolution and simplified N_2O_5 hydrolysis parameterizations (Milousis et al., 2025b). Ammonium aerosol is also overpredicted, with NMB values of +153 % at IMPROVE and +32 % at EANET (Fig. S9, Table S1), consistent with the nitrate bias and uncertainties in NH_3 emissions (Wang et al., 2025). Organic aerosols (OA) are systematically underpredicted across all networks. The largest bias is seen in the EPA urban dataset (NMB = −50 %), followed by EMEP (−39 %) and EANET (−38 %). This underestimation (Fig. S10, Table S1) has been linked to the absence of detailed biomass burning emissions and associated SOA formation pathways in the model (Tsimpidi et al., 2024). Root Mean Square Error (RMSE) values further highlight model uncertainty, especially for nitrate, with RMSEs of 0.8 μg m^{-3} (EPA), 2.81 μg m^{-3} (IMPROVE), and 2.08 μg m^{-3} (EANET). These elevated RMSE values reflect the greater variability and challenges in reproducing nitrate dynamics, particularly in rural and colder regions (Table S1).

Overall, the model captures the spatial and temporal variability of inorganic aerosols relatively well, particularly sulfate. However, it exhibits a consistent tendency to overestimate nitrate and ammonium and underestimate OA, patterns consistent with previous EMAC evaluations. These biases are attributed to both observational artifacts and missing processes, such as nighttime oxidation of biomass burning emissions, especially over Europe (Tsimpidi et al., 2024). A more detailed evaluation of EMAC performance is provided in Tsimpidi et al. (2024).

4. Impact of emission changes on atmospheric trace gases during the COVID-19 pandemic

4.1. Nitrogen oxides

The simulated BAU global average surface concentration of NOx is 0.3 ppb (1.1 ppb over land). Eastern and South Asia exhibit the highest regional annual average surface concentrations (~3 ppb), while the lowest levels are simulated over Eurasia (0.5 ppb). Under the CONFORM scenario, global average NOx concentrations decrease by 0.05 ppb (5 %; Fig. S3; Table 2) over land, consistent with the findings of Keller et al. (2021). In February, Eastern Asia experiences a significant NOx concentration reduction of 1 ppb (25 %) (Fig. 3b and c), primarily due to substantial emission decreases from transportation (40 %) and industry (30 %) (Fig. 1 and S1), which is comparable to the 27 % decrease reported by Zheng et el. (2021). This represents the highest reduction of the year for the region, although global average reductions during February remain the lowest (0.08 ppb or 5 %) as emissions elsewhere are largely like BAU levels. By April, lockdown enforcement worldwide leads to the highest global average NOx concentration reduction of the year (0.12 ppb or 12 %), despite a rebound in Eastern Asia due to increased industrial production and shipping activities (Fig. S1 and S2). Additional factors such as elevated residential sector emissions (Venter et al., 2020) and shifts in transportation patterns (Chang et al., 2021) may have further contributed to this regional increase. Over Eastern Asia, NOx concentrations decline only during February and March before gradually rising, peaking with a 10 % increase in November (Fig. 3b and f), a rebound effect also noted by Niu et al. (2022) for NO_2 emissions in China. In Southern Asia, NOx concentrations slightly increase (3 %) in December but remain below BAU levels for most of the year, with a maximum reduction of 27 % in April. This is consistent with the findings of Gopikrishnan et al. (2022), who observed a 21–36 % reduction in NO_2 levels across several Indian cities, followed by a subsequent increase in concentrations after the lockdown period. Europe experiences the steepest NO_x concentration decline, with a 31 % reduction in April (Fig. 3b and d), consistent with findings by Sekiya et al. (2023) and Deroubaix et al. (2021). This result also closely aligns with the 33 % average reduction reported for Europe by Keller et al. (2021). On an annual average in Europe, NO_x concentrations decrease by 10 % compared to BAU (Table 2). Significant annual reductions of around 10 % are also observed over Latin America, notably in major urban areas such as São Paulo and Mexico City, as well as in the Caribbean and the Middle East (Fig. 3d), whereas smaller reductions occur over Africa and Eurasia (3 %). North America experienced an annual decrease around 6 % (Table 2), with the highest reduction in April (14 %), particularly in the northeastern US (Fig. 3d).

Table 2
Percentage monthly and annual difference (%) of gas pollutant concentrations between COVID-19 and BAU scenario during the year 2020. A negative result indicates a decrease during COVID-19.

	O_3					NO_x					SO_2				
	Feb.	*Apr.*	*Jul.*	*Nov.*	*Ann.*	*Feb.*	*Apr.*	*Jul.*	*Nov.*	*Ann.*	*Feb.*	*Apr.*	*Jul.*	*Nov.*	*Ann.*
North America	−0.2	−1.5	−0.7	0.2	−0.6	−0.4	−14	−3.2	−10.9	−6.3	−4.0	−10.4	−3.2	3.3	−3.0
Europe	−0.2	−1.6	−1.1	2.4	−0.3	−0.3	−30.8	−4.6	−12.9	−9.6	−0.8	−14.6	−6.8	−9.2	−7.3
Eastern Asia	4.0	−2.1	−0.7	−3.0	−1.1	−25.3	0.9	2.2	10.3	0.1	−13.5	2.7	8.7	10.8	5.1
Southern Asia	−0.2	−3.4	−1.5	−0.5	−1.4	0.5	−27.3	−10.4	−3.0	−8.1	0.1	−20.7	−7.8	−1.0	−5.8
Eurasia	−0.1	−1.7	−0.7	0.3	−0.6	−0.8	−8.8	−1.3	−5.8	−3.0	−0.8	−19.1	−6.0	−11.0	−7.9
South-East Asia and Developing Pacific	−0.3	−2.6	−1.6	−0.8	−1.4	−0.9	−9.3	−5.8	−3.8	−4.8	−1.9	−11.8	−5.1	4.7	−3.1
Asia-Pacific Developed	0.0	−1.2	−1.3	−0.8	−0.9	0.1	−4.2	−3.3	−1.4	−2.4	0.7	−13.1	−6.3	−1.5	−4.3
Middle East	−0.2	−3.3	−1.6	−0.9	−1.4	0.0	−20.8	−10.9	−8.0	−9.8	−0.1	−11.3	−4.6	−3.8	−4.9
Africa	−0.2	−2.2	−1.1	−0.7	−1.0	−0.1	−9.8	−4.1	−1.5	−3.3	−0.2	−7.1	−1.6	−1.7	−2.3
Latin America & Caribbean	−0.1	−2.6	−1.8	−1.1	−1.4	−0.1	−19.2	−16.8	−7.2	−10.3	−0.7	−13.8	−7.8	−2.8	−5.7

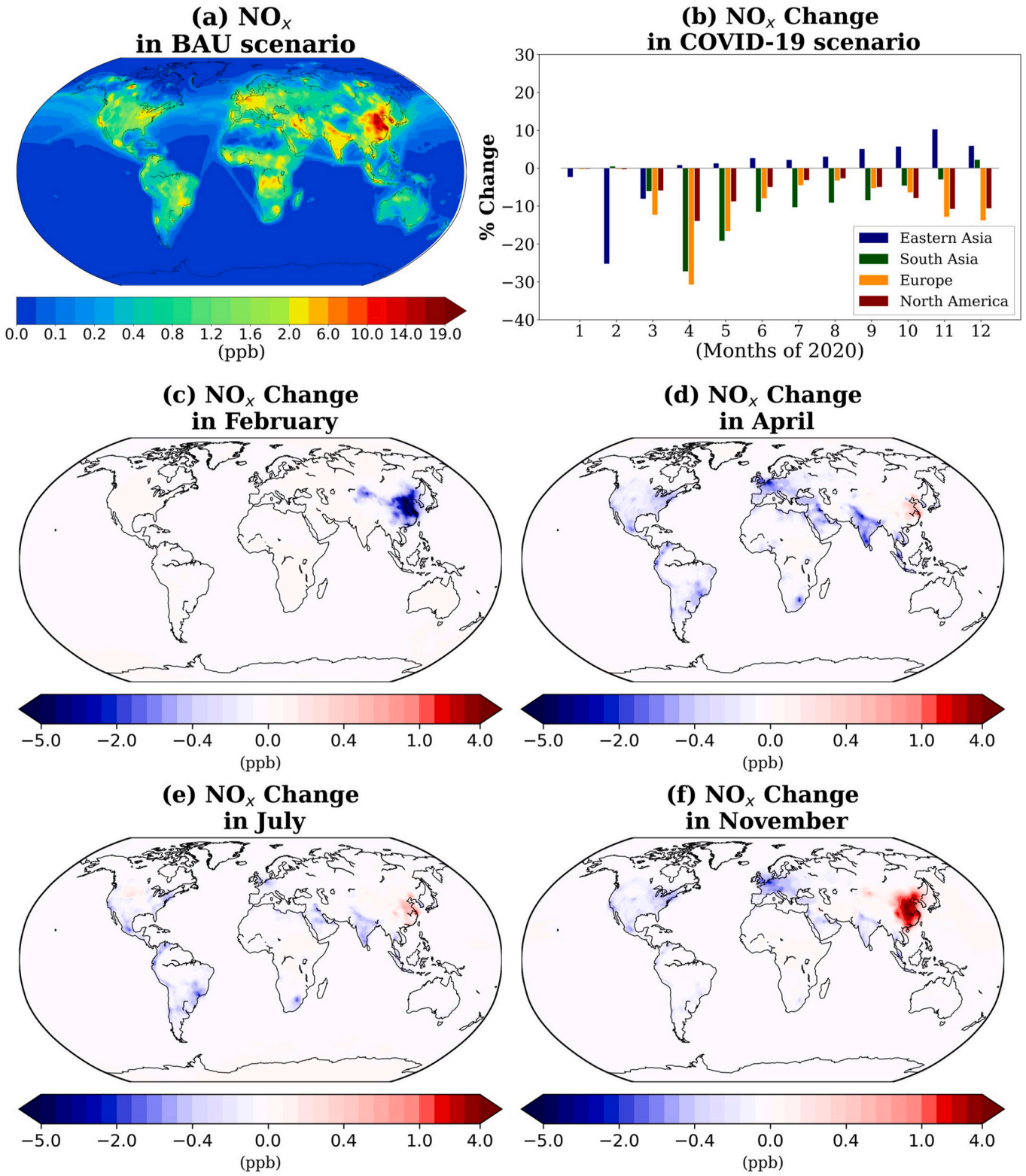

Fig. 3. **(a)** Annual average NO_x concentration (ppb) in the BAU scenario, **(b)** monthly average NO_x concentration change (%) during 2020 at specific locations and monthly average spatial NO_x concentration change (ppb) in **(c)** February, **(d)** April, **(e)** July and **(f)** November between BAU and COVID-19 and scenario; a negative change (blue) corresponds to a decrease in NO_x concentration during COVID-19. (For interpretation of the references to colour in this figure legend, the reader is referred to the Web version of this article.)

4.2. Ozone

The BAU simulated global annual average surface concentration of O_3 is 36.6 ppb (42 ppb over land). The area of Southern Asia has the highest annual average surface concentration of O_3 (61.1 ppb), followed by the Middle East (59.1 ppb), while the lowest O_3 concentrations are simulated over the Asia-Pacific Developed region (33.3 ppb annual average). For North America, Europe, and East Asia the annual surface

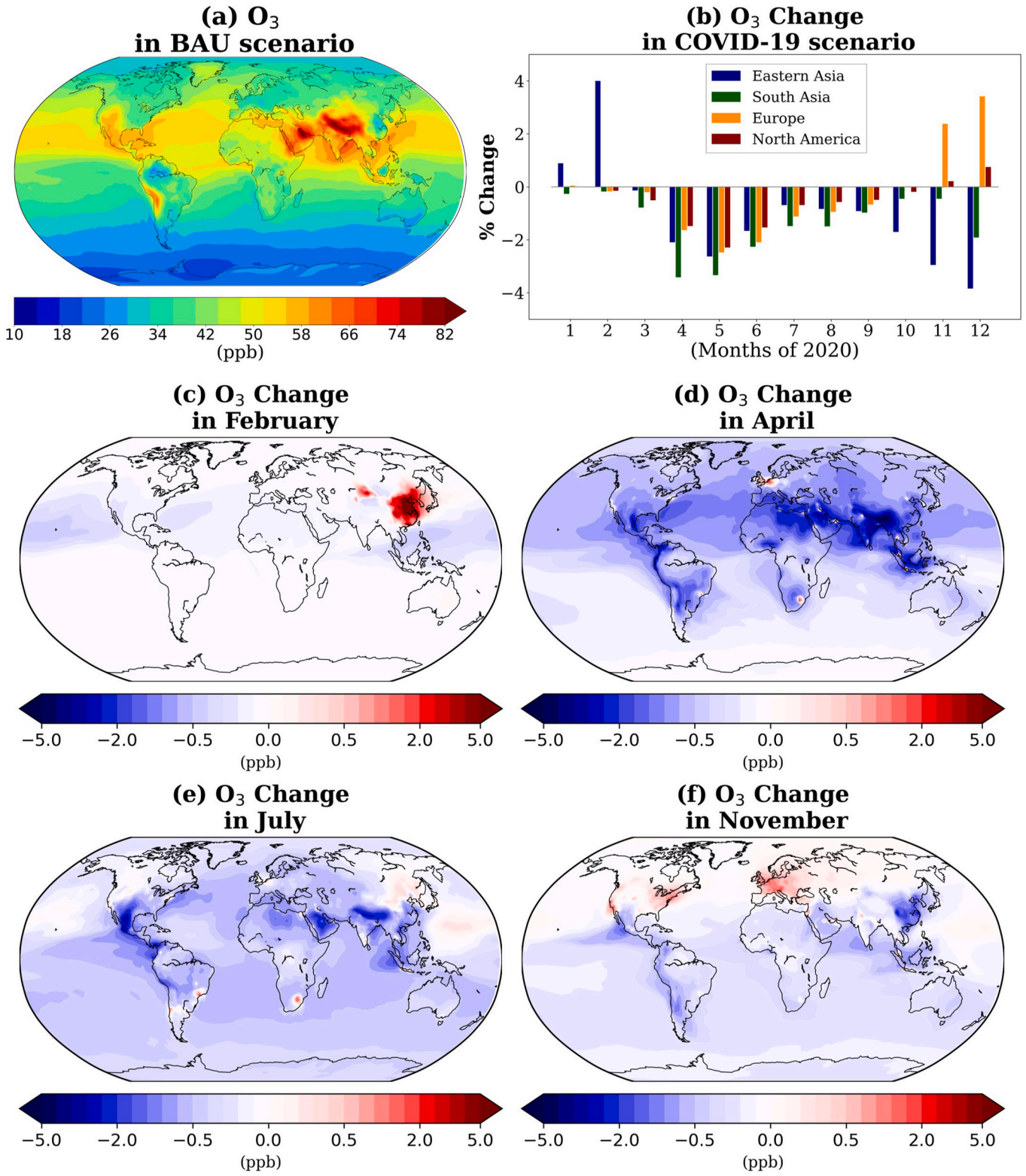

Fig. 4. **(a)** Annual average O_3 concentration (ppb) in the BAU scenario, **(b)** monthly average O_3 concentration change (%) during 2020 at specific locations and monthly average spatial O_3 concentration change (ppb) in **(c)** February, **(d)** April, **(e)** July and **(f)** November between BAU and COVID-19 and scenario; a negative change (blue) corresponds to a decrease in O_3 concentration during COVID-19. (For interpretation of the references to colour in this figure legend, the reader is referred to the Web version of this article.)

concentrations are 40.2 ppb, 37.8 ppb, and 49.8 ppb, respectively (Fig. 4a).

Using the CONFORM emission adjustment factors to account for emission changes during the COVID-19 pandemic (CONFORM simulation scenario), the simulated global annual average O_3 concentration over land decreased by 0.3 ppb (0.8 %; Fig. S3). The largest decrease was simulated in the month of May (−1.2 ppb, or 2.5 %), while in February the global average O_3 concentration was increased by 0.04

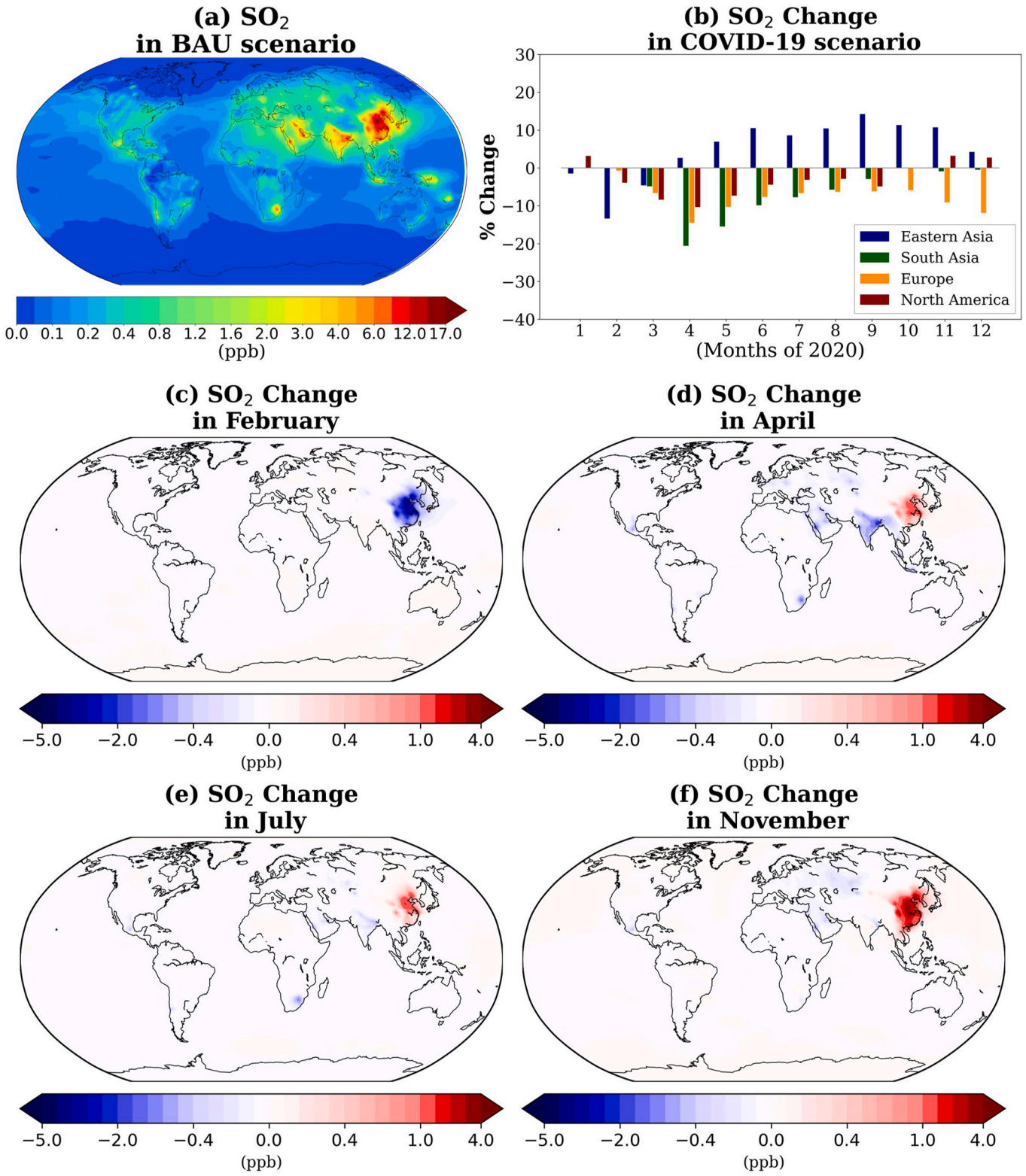

Fig. 5. **(a)** Annual average SO_2 concentration (ppb) in the BAU scenario, **(b)** monthly average SO_2 concentration change (%) during 2020 at specific locations and monthly average spatial SO_2 concentration change (ppb) in **(c)** February, **(d)** April, **(e)** July and **(f)** November between BAU and COVID-19 and scenario; a negative change (blue) corresponds to a decrease in SO_2 concentration during COVID-19. (For interpretation of the references to colour in this figure legend, the reader is referred to the Web version of this article.)

ppb (0.2 %). During February, changes in O_3 precursor emissions are minimal around the world, except for Eastern Asia, where the first lockdowns were enforced to prevent the spread of the new pandemic (Fig. 4b; Table 2). The densely populated urban areas of Eastern Asia are characterized by high NO_x concentrations. In such NO_x-saturated environments (i.e., low VOC/NO_x ratio), the drastic reduction in NO_x emissions can lead to a decrease in O_3 titration and thus an increase in O_3 concentration (Fig. S4). The simulated O_3 concentration over Eastern

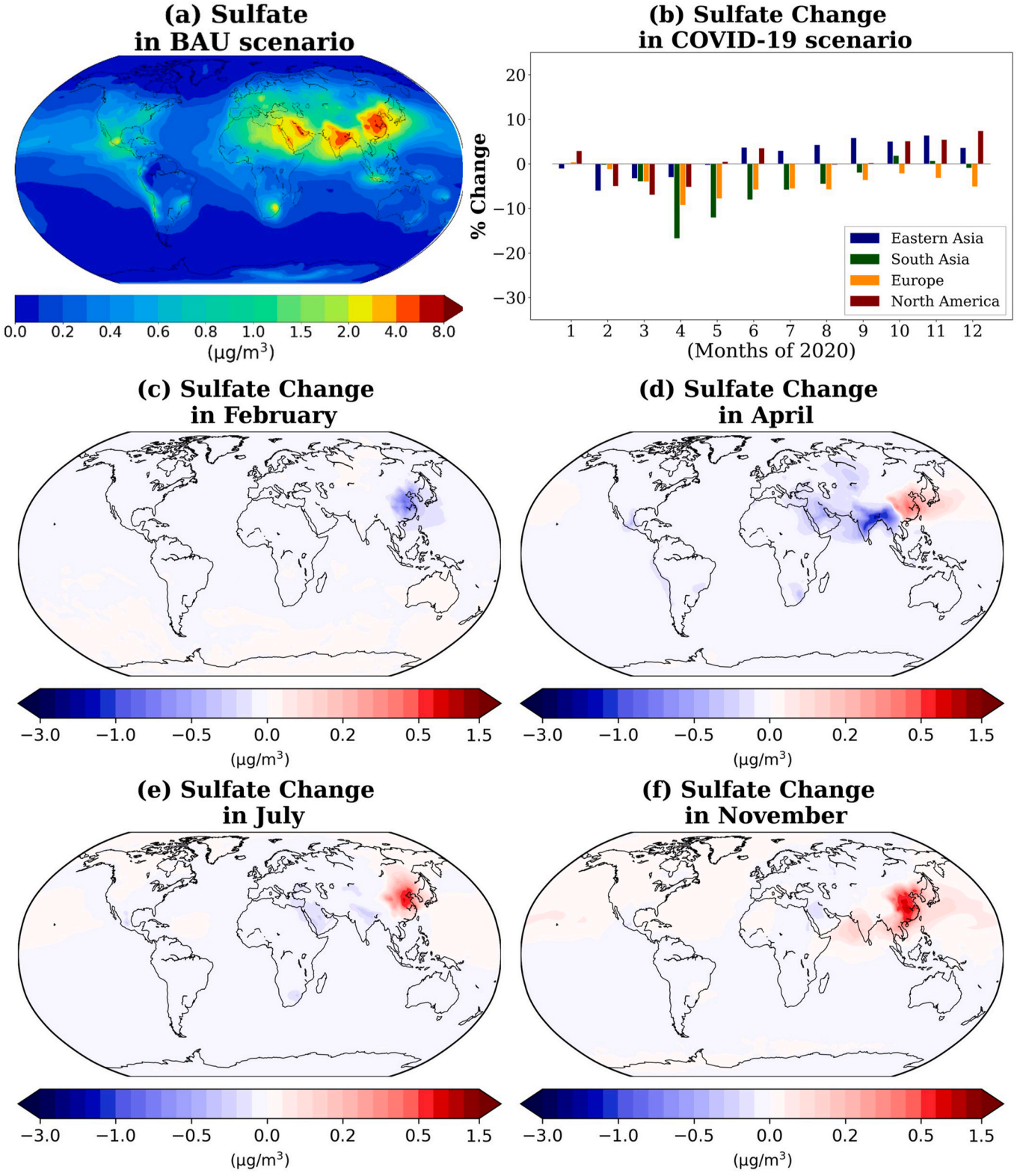

Fig. 6. **(a)** Annual average $PM_{2.5}$-Sulfate concentration (μg m^{-3}) in the BAU scenario, **(b)** monthly average $PM_{2.5}$-Sulfate concentration change (%) during 2020 at specific locations and monthly average spatial $PM_{2.5}$-Sulfate concentration change (μg m^{-3}) in **(c)** February, **(d)** April, **(e)** July and **(f)** November between BAU and COVID-19 and scenario; a negative change (blue) corresponds to a decrease in $PM_{2.5}$-Sulfate concentration during COVID-19. (For interpretation of the references to colour in this figure legend, the reader is referred to the Web version of this article.)

Table 3
Percentage monthly and annual difference (%) of inorganic aerosol pollutant concentrations between COVID-19 and BAU scenario during the year 2020. A negative result indicates a decrease during COVID-19.

	Sulfate					Nitrate					Ammonium				
	Feb.	*Apr.*	*Jul.*	*Nov.*	*Ann.*	*Feb.*	*Apr.*	*Jul.*	*Nov.*	*Ann.*	*Feb.*	*Apr.*	*Jul.*	*Nov.*	*Ann.*
North America	−5.1	−5.2	0.0	5.5	0.6	−2.5	−10.8	−1.3	−4.6	−4.4	−3.6	−11.2	−1.7	−2.8	−2.5
Europe	−1.2	−9.3	−5.6	−3.2	−4.5	−0.8	−26.6	−7.4	−8.7	−9.4	−0.8	−24.7	−8.6	−6.8	−8.6
Eastern Asia	−6.1	−3.1	3.0	6.4	1.5	−14.6	−1.0	2.4	1.1	−0.9	−11.9	−4.6	4.3	2.9	0.0
Southern Asia	−0.3	−16.8	−5.9	0.7	−4.3	0.2	−19.0	−8.3	−2.4	−6.1	0.0	−33.2	−10.1	−1.2	−8.2
Eurasia	−1.0	−13.2	−2.6	−6.8	−4.9	−1.3	−12.5	−1.5	−3.3	−3.3	−1.1	−19.2	−3.7	−4.7	−6.1
South-East Asia and Developing Pacific	−2.0	−9.6	−3.4	2.5	−2.7	−2.1	−13.8	−2.3	0.7	−3.6	−2.2	−12.0	−5.7	2.0	−4.3
Asia-Pacific Developed	0.3	−10.1	−4.3	−2.2	−3.9	−0.5	−1.2	−3.3	−0.2	−1.9	1.8	11.6	−0.5	−0.9	2.0
Middle East	−0.4	−11.6	−5.0	−2.2	−4.1	−0.4	−6.0	−2.5	−3.1	−0.8	−0.5	−27.3	−9.9	−3.8	−8.4
Africa	−0.5	−8.7	−2.5	−1.1	−3.0	−0.2	0.0	−0.6	−1.0	−0.6	−0.5	−12.2	−3.6	−2.3	−4.7
Latin America & Caribbean	−0.5	−11.6	−6.2	−2.4	−4.7	−0.1	−6.0	−7.9	−3.0	−4.5	−0.4	−15.1	−11.0	−4.9	−7.2

Asia during February is increased by 4 % on a regional average (Table 2). These findings are consistent with the results of Le et al. (2020) and Venter et al. (2020) as well as with the results of many field observations during this period as summarized by Gkatzelis et al. (2021a). Increases in O_3 concentrations are also evident after April, when lockdowns began to be enforced, in several polluted regions of central Europe, consistent with the findings of Cuesta et al. (2022), northeastern US and California, in agreement with Campbell et al. (1994) and Wang et al. (2024) (Fig. 4d). Similar increases are observed in Latin America, particularly in São Paulo (Fig. 4d and e), in South Africa (Fig. 4d and e; Keller et al., 2021), and in Southern Asia, especially in New Delhi (Fig. 4e and f), consistent with the findings of Gopikrishnan et al. (2022). However, the largest O_3 increases are simulated in November and December (Figs. S5 and 4b) by 2.4 % and 3.4 %, respectively, over Europe and by 0.2 % and 0.8 %, respectively, over North America, when the lockdowns were reinforced to combat the second wave of the pandemic, and the winter NOx-saturated conditions further favor the increase of O_3 after the reduction of NO_x emissions (Fig. S4). On the other hand, over areas with higher VOC/NOx ratios (e.g., NOx-limited rural environments) a decrease in NOx emissions can lead to a decrease in O_3 concentrations (Fig. S4). Simulated regional annual average O_3 concentrations decreased by up to 1.4 % in Southern Asia (1 ppb), South-East Asia and Developing Pacific (0.7 ppb), Latin America and the Caribbean (0.5 ppb), and the Middle East (0.9 ppb). In Southern Asia, the largest decrease (2.5 ppb, or 3.4 %) is simulated in April, in agreement with Gaubert et al. (2021) and Huang et al. (2021), and the smallest decrease (0.2 ppb, or 0.5 %) is simulated in October and November.

4.3. Sulfur dioxide

The global annual average SO_2 concentration is 0.24 ppb (0.65 ppb over land), with the highest concentrations simulated over the densely populated areas of Eastern and Southern Asia (2.72 ppb regional average; Fig. 5a). On the other hand, North America has the lowest regional average SO_2 concentration of 0.15 ppb due to the drastic reduction of its emissions over the last 40 years.

According to the CONFORM simulation scenario, the global annual average SO_2 concentration over land decreases by 4 % (Fig. S3), which is in line with the 2 % decline observed by Amritha et al. during the April–May 2020 period. The main sources of SO_2 are emissions from industry and the energy sector. Industrial activity was severely affected during the quarantine period, while the energy sector was least affected by the closures during the COVID-19 pandemic, as the reduction in energy demand from commercial buildings was offset by an increase in demand from households (Zheng et al., 2021). Nevertheless, global average SO_2 emissions were reduced by 12 % in April, following large SO_2 reductions in most locations except East Asia (Fig. 5b and d; Table 2). An increasing effect dominates East Asia after April, with the highest increase in September (14.3 %; Fig. 5b). A similar effect is reported by Zheng et al. (2020) and Liu et al. (2020). Increased industrial production and shipping are the main reasons for this post-quarantine recovery (Fig. 1 and S1; Fig. 5b and d). The most significant SO_2 decrease occurs over Southern Asia and Eurasia during April (20 %), confirming the results of Amritha et al. (2024) and Sekiya et al. (2023). Meanwhile, the Middle East and Latin America and the Caribbean experience a significant decrease in April (11–14 %). The SO_2 reduction over South Asia tapers off after April, reaching BAU levels by the end of the summer. The only regions that continue to show significant SO_2 reductions until the end of the year (around 10 %) are Europe (Fig. 5b) and Eurasia (Table 2). In the remaining regions, SO_2 concentrations after November are in the range of BAU levels (e.g., Africa, developed Asia-Pacific) or even higher (e.g., East Asia, North America).

5. Impact of emission changes on atmospheric aerosols during the COVID-19 pandemic

5.1. Sulfate

The global average surface concentration of sulfate aerosol is 0.33 μg m^{-3} (0.7 μg m^{-3} over land). Sulfate concentrations peak over Southern Asia (regional average of 3 μg m^{-3}), followed by the Middle East (2.4 μg m^{-3}) and Eastern Asia (1.9 μg m^{-3}). On the contrary, the lowest concentrations are calculated over North America (0.2 μg m^{-3}) due to the strong reduction of SO_2 emissions as discussed in section 4.3. The global annual average sulfate concentration over land decreased by 3 % (Fig. S3) after considering the emission reduction due to the lockdowns in 2020. Following the changes in SO_2 concentrations, sulfate decreases by 17 % over Eastern Asia in February. Since North America is affected by the long-range transport of gas-phase pollutants from Eastern Asia (Jaffe et al., 1999; Karydis et al., 2012; Lin et al., 2014), the sulfate concentration over North America also decreases during February, even though the local authorities have not yet imposed lockdowns (Fig. 6b, Table 3). After the global spread of COVID-19, sulfate concentrations begin to decrease in each region, reaching a maximum global average decrease of 9 % (−0.1 μg m^{-3}) in April. During April, the largest decrease is simulated over Southern Asia (17 % regional average), while the smallest decrease is simulated over Eastern Asia (3 % regional average), as sulfate increases in many parts of Eastern Asia due to the increase in Industrial emissions and shipping (Fig. 6b and d, Fig. 1 and S1). Le et al. (2020) also report that an induced reduction in NO_x emissions has led to an increase in sulfate aerosol over China. The increase in sulfate over Eastern Asia intensifies towards the end of the year (reaching 6 % in November), leading to an increase in sulfate in regions affected by transported pollution (e.g., Southeast Asia and developing Pacific, North America; Fig. 6 and Table 3). Over Europe, sulfate decreases significantly during the first phase of the pandemic (9 % in April), in accordance with Sekiya et al. (2023), but only slightly during the second phase (3 % in November) despite the strong decrease in SO_2 (section 4.3), mainly due to increased precipitation and reduced

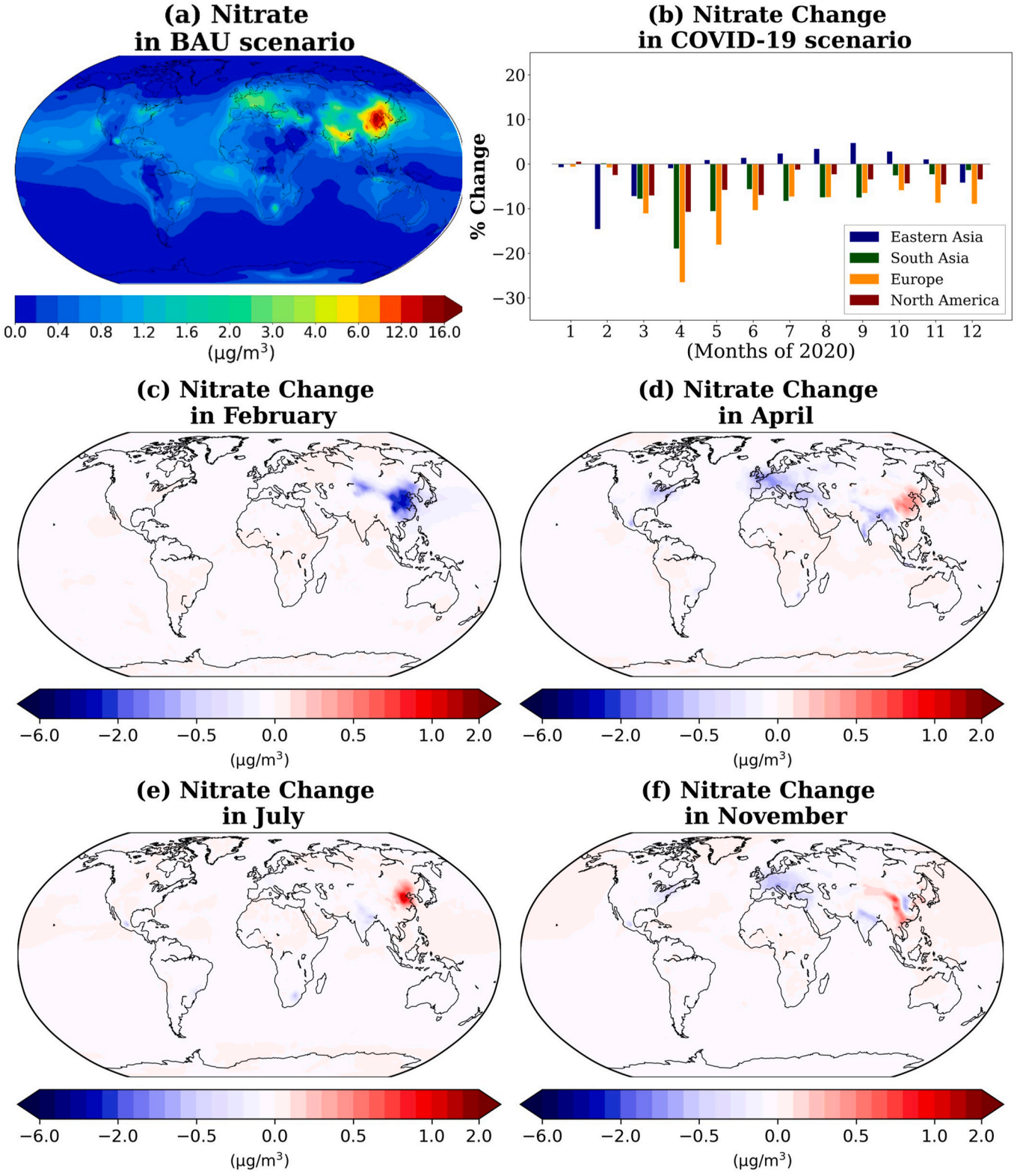

Fig. 7. **(a)** Annual average $PM_{2.5}$-Nitrate concentration (μg m^{-3}) in the BAU scenario, **(b)** monthly average $PM_{2.5}$-Nitrate concentration change (%) during 2020 at specific locations and monthly average spatial $PM_{2.5}$-Nitrate concentration change (μg m^{-3}) in **(c)** February, **(d)** April, **(e)** July and **(f)** November between BAU and COVID-19 and scenario; a negative change (blue) corresponds to a decrease in $PM_{2.5}$-Nitrate concentration during COVID-19. (For interpretation of the references to colour in this figure legend, the reader is referred to the Web version of this article.)

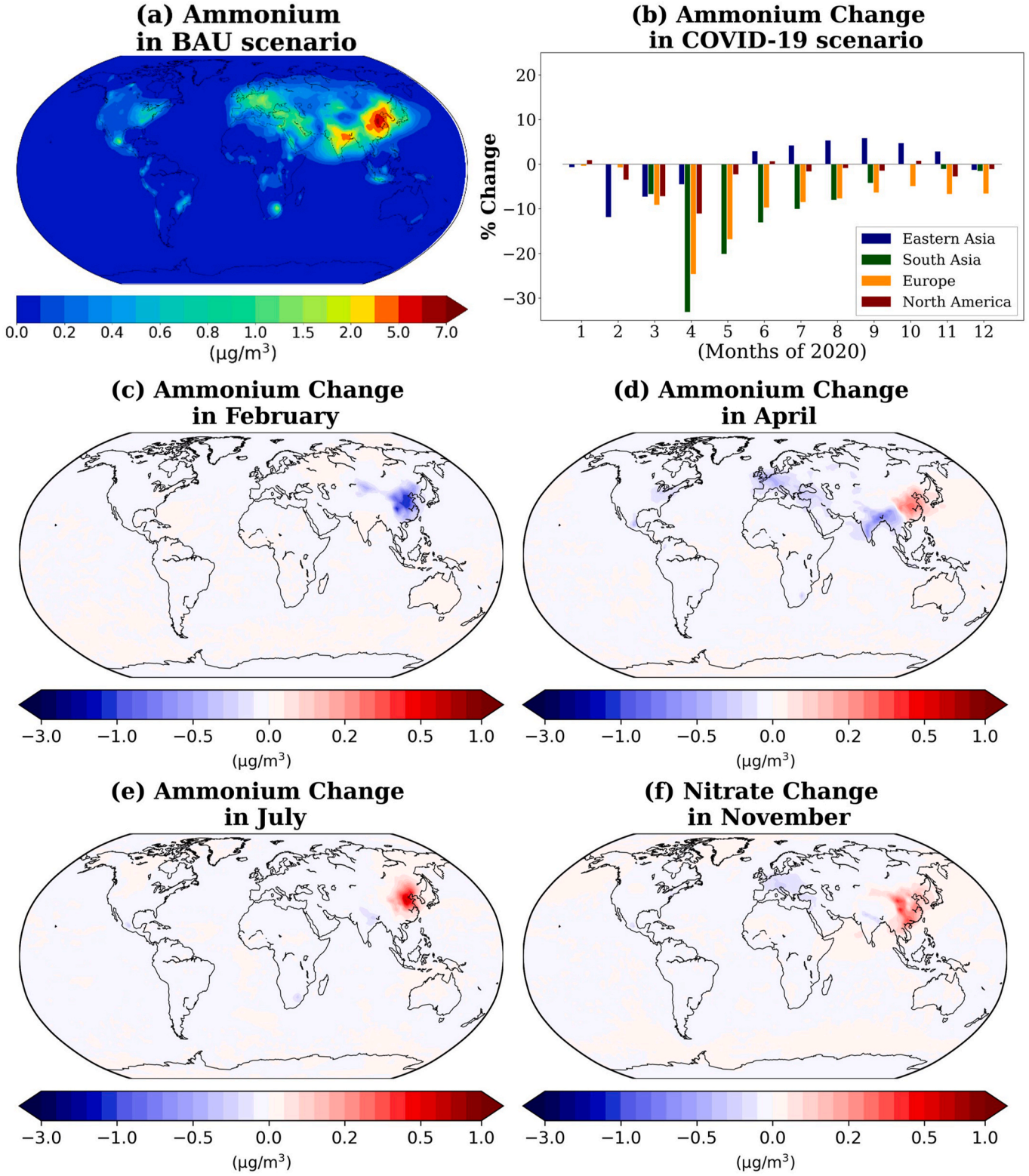

Fig. 8. **(a)** Annual average $PM_{2.5}$-Ammonium concentration (μg m^{-3}) in the BAU scenario, **(b)** monthly average $PM_{2.5}$-Ammonium concentration change (%) during 2020 at specific locations and monthly average spatial $PM_{2.5}$-Ammonium concentration change (μg m^{-3}) in **(c)** February, **(d)** April, **(e)** July and **(f)** November between BAU and COVID-19 and scenario; a negative change (blue) corresponds to a decrease in $PM_{2.5}$-Ammonium concentration during COVID-19. (For interpretation of the references to colour in this figure legend, the reader is referred to the Web version of this article.)

photochemistry. In addition, the increased O_3 concentrations and other atmospheric oxidants (e.g., OH^-, H_2O_2) during November (see section 4.1) accelerated the gaseous and aqueous phase production of H_2SO_4, which compensated for the decreased SO_2 emissions (Fig. S5). This aligns with Wang et al. (2024), who emphasized heterogeneous chemistry, especially under humid and polluted conditions, as a significant contributor to sulfate formation.

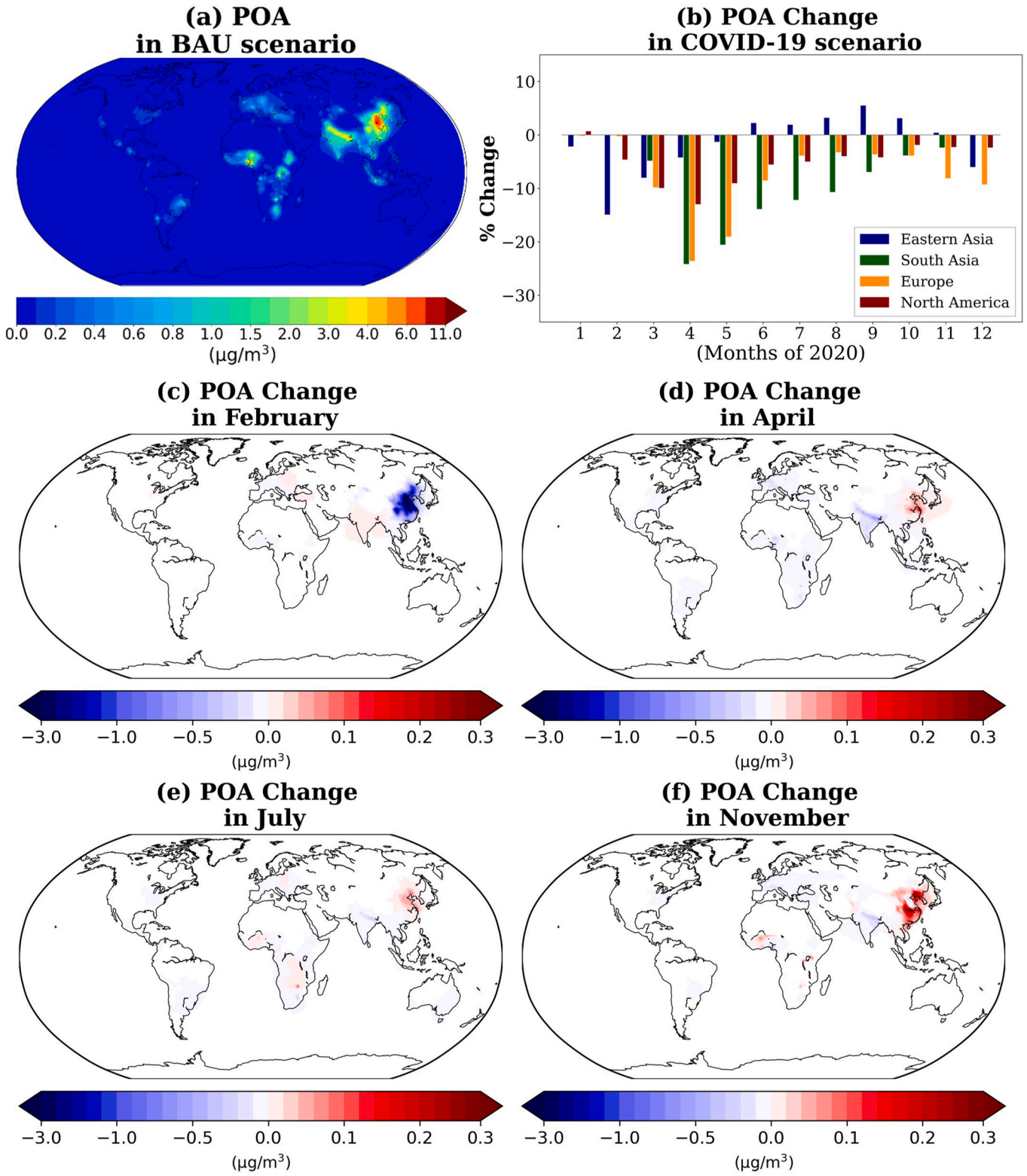

Fig. 9. **(a)** Annual average $PM_{2.5}$-POA concentration (μg m^{-3}) in the BAU scenario, **(b)** monthly average $PM_{2.5}$-POA concentration change (%) during 2020 at specific locations and monthly average spatial $PM_{2.5}$-POA concentration change (μg m^{-3}) in **(c)** February, **(d)** April, **(e)** July and **(f)** November between BAU and COVID-19 and scenario; a negative change (blue) corresponds to a decrease in $PM_{2.5}$-POA concentration during COVID-19. (For interpretation of the references to colour in this figure legend, the reader is referred to the Web version of this article.)

Table 4
Percentage monthly and annual difference (%) of anthropogenic organic aerosol pollutant concentrations between COVID-19 and BAU scenario during the year 2020. A negative result indicates a decrease during COVID-19.

	POA					SOA from S/IVOC					SOA from VOC				
	Feb.	*Apr.*	*Jul.*	*Nov.*	*Ann.*	*Feb.*	*Apr.*	*Jul.*	*Nov.*	*Ann.*	*Feb.*	*Apr.*	*Jul.*	*Nov.*	*Ann.*
North America	−4.7	−13.0	−5.1	−2.3	−5.1	−6.2	−8.5	−2.2	2.0	−2.3	−5.4	−10.6	−4.5	1.9	−3.4
Europe	−0.3	−23.6	−3.9	−8.2	−7.8	−1.8	−17.3	−3.5	−3.8	−5.6	−2.1	−19.5	−5.8	−4.7	−7.0
Eastern Asia	−15.0	−4.3	2.0	0.5	−1.7	−5.9	−4.7	2.1	−1.2	−1.1	−6.6	−4.9	2.8	1.3	−0.2
Southern Asia	0.1	−24.2	−12.2	−2.4	−8.3	−0.2	−17.8	−8.1	−2.9	−6.4	−0.2	−20.1	−9.2	−2.9	−7.2
Eurasia	−1.9	−18.5	−0.1	−5.3	−5.3	−1.6	−13.2	1.0	−3.4	−3.8	−1.4	−15.0	−1.1	−3.4	−4.6
South-East Asia and Developing Pacific	−1.6	−9.7	−2.8	−0.1	−3.2	−1.9	−8.5	−3.4	−0.5	−3.3	−1.8	−8.9	−4.6	0.7	−3.5
Asia-Pacific Developed	0.7	−15.4	−1.8	−7.5	−5.8	0.5	−8.8	−2.4	−3.1	−3.6	0.3	−9.1	−4.2	−2.6	−4.1
Middle East	−0.3	−19.9	−9.2	−4.3	−7.9	−0.7	−12.4	−5.4	−2.8	−4.7	−0.8	−18.0	−8.9	−4.6	−7.3
Africa	−0.3	−10.8	−2.7	−2.0	−3.3	−0.5	−9.5	−2.4	−1.8	−3.1	−0.6	−11.2	−4.1	−2.9	−4.3
Latin America & Caribbean	−0.3	−14.8	−11.9	−5.2	−7.9	−0.4	−11.3	−8.0	−3.5	−5.7	−0.4	−14.8	−10.9	−5.2	−7.7

5.2. Nitrate

The simulated global annual average surface nitrate aerosol concentration is 0.4 μg m^{-3} (0.8 μg m^{-3} over land). The highest regional average concentrations are simulated over Eastern Asia (3.6 μg m^{-3}) and Southern Asia (3 μg m^{-3}). Following the sharp reduction in NO_x emissions during the 2020 lockdowns (Section 2.3), global annual average nitrate concentrations over land decreased by 3 % (Fig. S3). Over Eastern Asia, nitrate decreases by 15 % in February and 1 % in April, before increasing again relative to BAU levels, peaking at a 2.5 % increase in summer (Fig. 7b, Table 3). The largest decrease in nitrate concentrations is simulated over Europe (27 % in April; Fig. 7; Table 3). Over Europe in BAU, the fraction of total nitric acid present in the aerosol phase is high (annual average of 83 %; Fig. S6) due to the high availability of NH_3 in the region. Therefore, the strong reduction of NO_x emissions (35 % in April) has a direct impact on nitrate aerosol formation in the region. The annual average reduction of nitrate in Europe is about 10 %. For the same reasons, nitrate is also significantly reduced over Southern Asia (6 % annual average) with a peak reduction of 19 % in April. On the other hand, nitrate reduction is low in areas where nitrate formation is limited by the availability of NH_3 (e.g., North America) and the high temperatures (e.g., Middle East) (Fig. S6; Table 3). Nitrate reduction is also low in areas where NO_x emission reduction is weak (e.g., Africa; Table 3). Furthermore, the increased oxidizing capacity due to NO_x reduction, could also lead to a relative increase in secondary aerosols, such as nitrate, within the aerosol composition (Liu et al., 2021b; Tian et al., 2021).

5.3. Ammonium

The simulated annual average surface concentration of ammonium aerosol is 0.1 μg m^{-3} (0.35 μg m^{-3} over land). The highest ammonium concentrations are simulated over Southern and Eastern Asia (1.7 and 1.5 μg m^{-3}, respectively). Although NH_3 emissions are not as affected by the 2020 lockdowns, in some cases an increase occurred due to the agricultural sector (Kuttippurath et al., 2024). The reduction in SO_2 and NO_x emissions affects the partitioning of NH_3 into the aerosol phase, resulting in a global annual decrease in continental ammonium concentrations of 4.5 % (Fig. S3). Viatte et al. (2023) attributed the decline to reduced emissions of NH_3 and NO_x from industrial activities and transportation. The largest annual reduction of ammonium is simulated over Europe (9 %) with a peak of 25 % in April (Fig. 8b, Table 3). Over Southern Asia, ammonium is reduced by 33 % in April, but the reduction weakens by the end of the year (1 %) due to the slight increase in sulfuric acid (section 5.1). The ammonium reduction is also significant over the Middle East (8 % annually) due to the significant reduction of sulfate in the region (Table 3). On the other hand, the reduction of ammonium in North America is weak, especially in the western USA (Fig. 8). Following the changes in sulfate and nitrate concentrations, ammonium decreases over East Asia in February (12 %) and April (5 %) and increases thereafter (Table 3).

5.4. POA and SOA from anthropogenic SVOC and IVOC

The global annual average surface concentration of POA and SOA from anthropogenic S/IVOC emissions is 0.05 μg m^{-3} (0.2 μg m^{-3} over land) and 0.1 μg m^{-3} (0.3 μg m^{-3} over land), respectively, with peaks over the regions of Southern Asia (1.2 μg m^{-3} POA and 2.4 μg m^{-3} SOA regional average) and Eastern Asia (1.1 μg m^{-3} POA and 0.7 μg m^{-3} SOA regional average). After application of the CONFORM emission adjustment factors, the global annual average POA and SOA from S/IVOC emissions over land are reduced by 5 % and 3.5 %, respectively (Fig. S3). Over Eastern Asia, POA concentrations decrease by 15 % in February and 4 % in April, and then increase, following the emission trends (Fig. 9; Table 4). SOA concentrations in Eastern Asia decrease by 6 % in February and 5 % in April and increase by 4 % in summer (Fig. 10; Table 4). However, in contrast to POA, SOA concentrations decrease again from BAU levels after October, despite the increase in S/IVOC emissions. This slight decrease is related to the lower atmospheric oxidant levels during this period, as discussed in section 4 (Fig. S5), which led to less efficient oxidation of the emitted S/IVOC and subsequent reduced SOA production. In April, POA and SOA concentrations decreased globally, with large decreases over Southern Asia and Europe (24 % for POA and 18 % for SOA) and over the Middle East (20 % for POA and 12 % for SOA) (Figs. 9 and 10, Table 4). Over Europe, POA and SOA reductions are small during the summer (4 % for both), and POA reductions become important again after November (8 %) during the second wave of the pandemic. However, the SOA reduction in November remains small (4 %), because of the dramatic increase in oxidant levels (Fig. S5). On the other hand, over Africa, POA and SOA concentrations over densely populated areas (e.g., Nigeria, and South Africa) increase slightly relative to BAU levels after July (Table 4) mainly due to increase in S/IVOC emissions from the residential sector (Fig. S2), consistent with the results of Han et al. (2024).

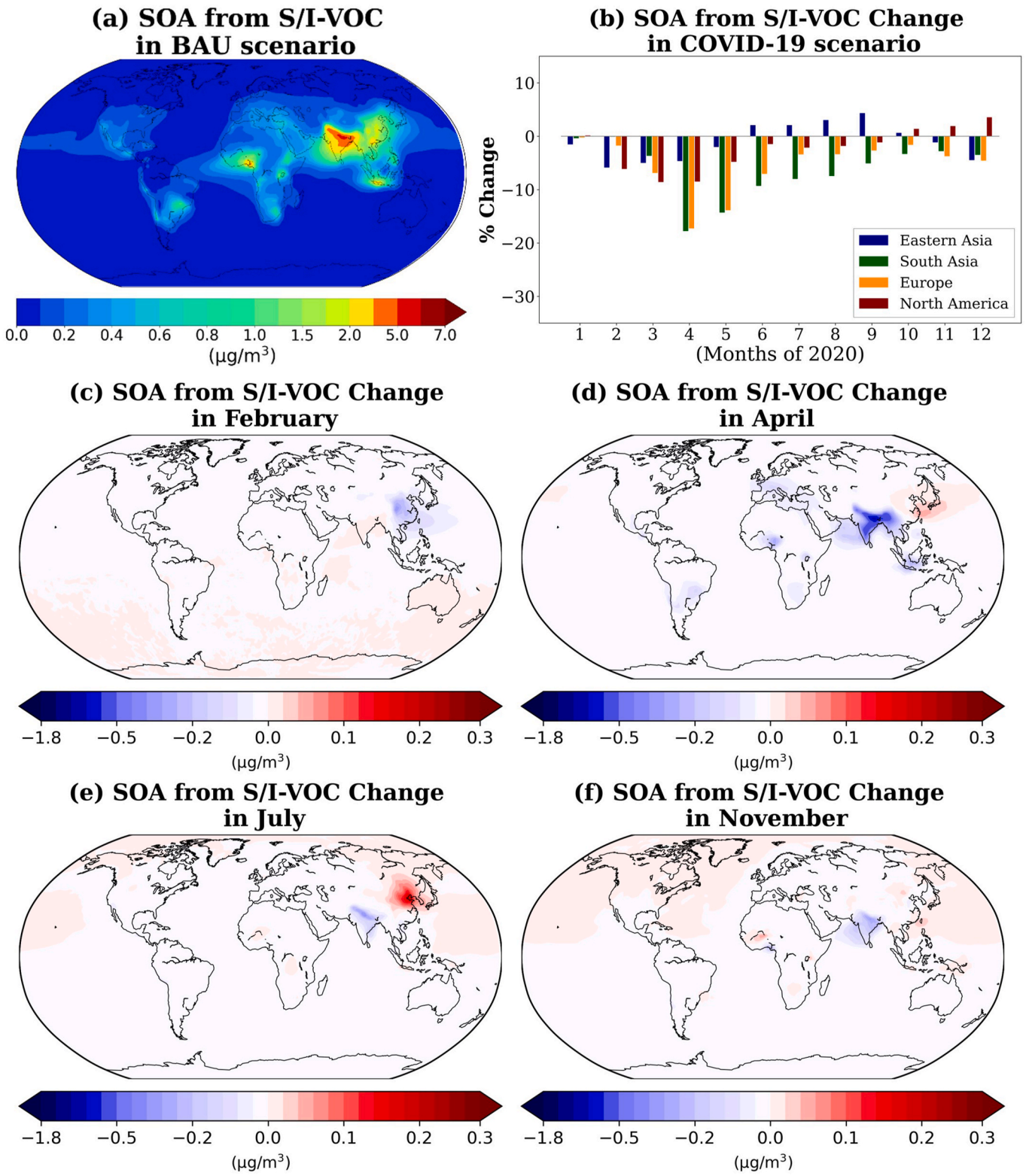

Fig. 10. **(a)** Annual average $PM_{2.5}$-SOA concentration (μg m^{-3}) from anthropogenic SVOC and IVOC emissions in the BAU scenario, **(b)** monthly average $PM_{2.5}$-SOA concentration change (%) during 2020 at specific locations and monthly average spatial $PM_{2.5}$-SOA concentration change (μg m^{-3}) in **(c)** February, **(d)** April, **(e)** July and **(f)** November between BAU and COVID-19 and scenario; a negative change (blue) corresponds to a decrease in $PM_{2.5}$-SOA concentration during COVID-19. (For interpretation of the references to colour in this figure legend, the reader is referred to the Web version of this article.)

5.5. SOA from anthropogenic VOCs

The global annual average surface concentration of SOA from anthropogenic VOC emissions is 0.2 μg m^{-3} (0.5 μg m^{-3} over land). The area of Southern Asia has the highest average surface concentration (3.5 μg m^{-3}), followed by South-East Asia and the Developing Pacific (1.6 μg m^{-3}) and Eastern Asia (1.7 μg m^{-3}). The lowest average concentration belongs to Asia-Pacific Developed (0.1 μg m^{-3}), followed by North

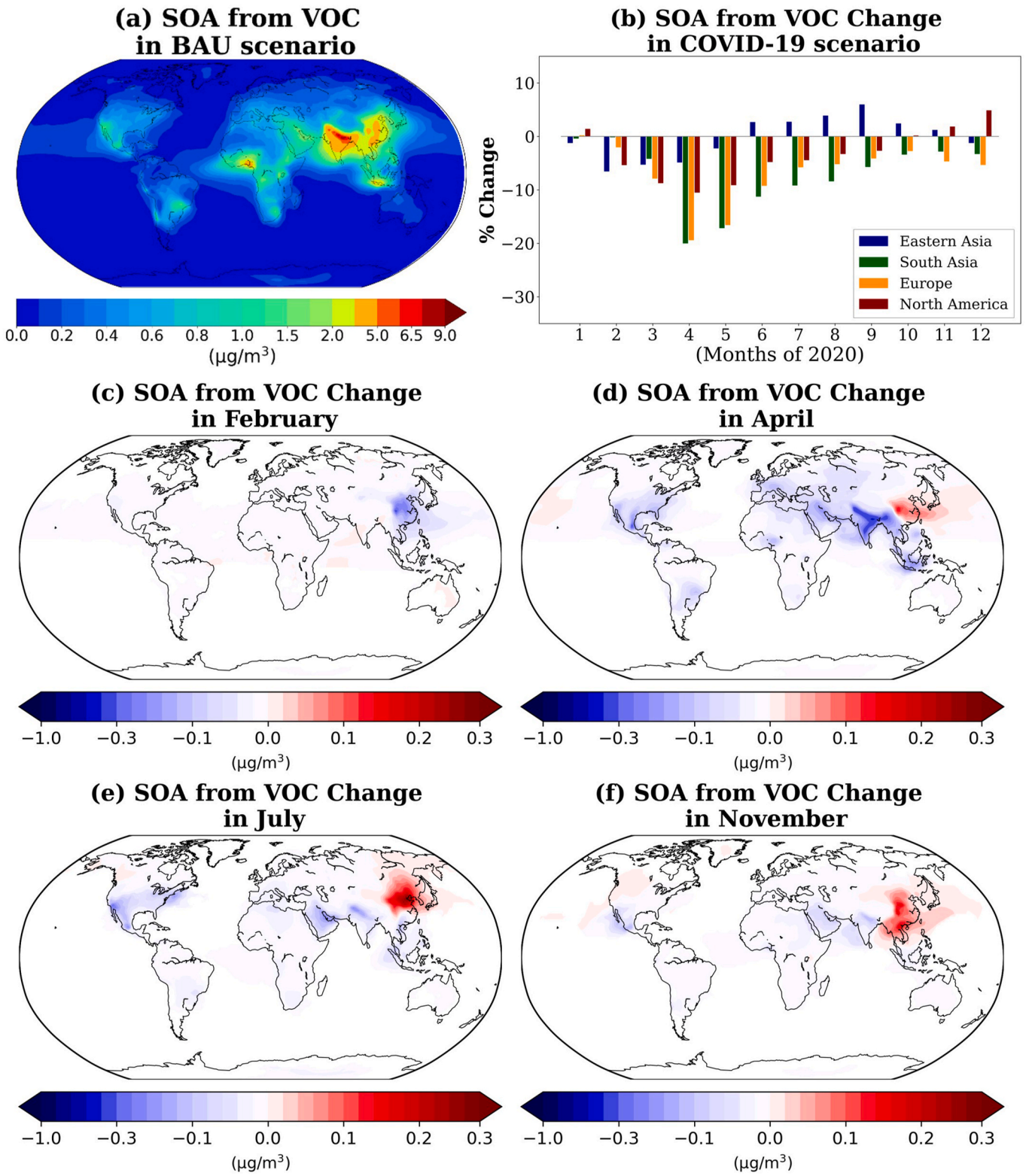

Fig. 11. **(a)** Annual average $PM_{2.5}$-SOA concentration (μg m^{-3}) from anthropogenic VOC emissions in the BAU scenario, **(b)** monthly average $PM_{2.5}$-SOA concentration change (%) during 2020 at specific locations and monthly average spatial $PM_{2.5}$-SOA concentration change (μg m^{-3}) in **(c)** February, **(d)** April, **(e)** July and **(f)** November between BAU and COVID-19 and scenario; a negative change (blue) corresponds to a decrease in $PM_{2.5}$-SOA concentration during COVID-19. (For interpretation of the references to colour in this figure legend, the reader is referred to the Web version of this article.)

America and Eurasia (0.2 μg m^{-3}). After applying the CONFORM emission adjustment factors, the global annual average SOA concentrations from anthropogenic VOCs over land are reduced by 4.5 % (Fig. S8). In Southern Asia, the largest decrease relative to BAU was calculated in April (20 %; Fig. 11b, Table 4). In addition, the smallest decrease was calculated in November (3 %; Fig. 11b and f). In Europe, the largest decrease occurred in April (20 %; Fig. 11b), while the smallest decrease was calculated in October (3 %; Fig. 11, Table 4), as

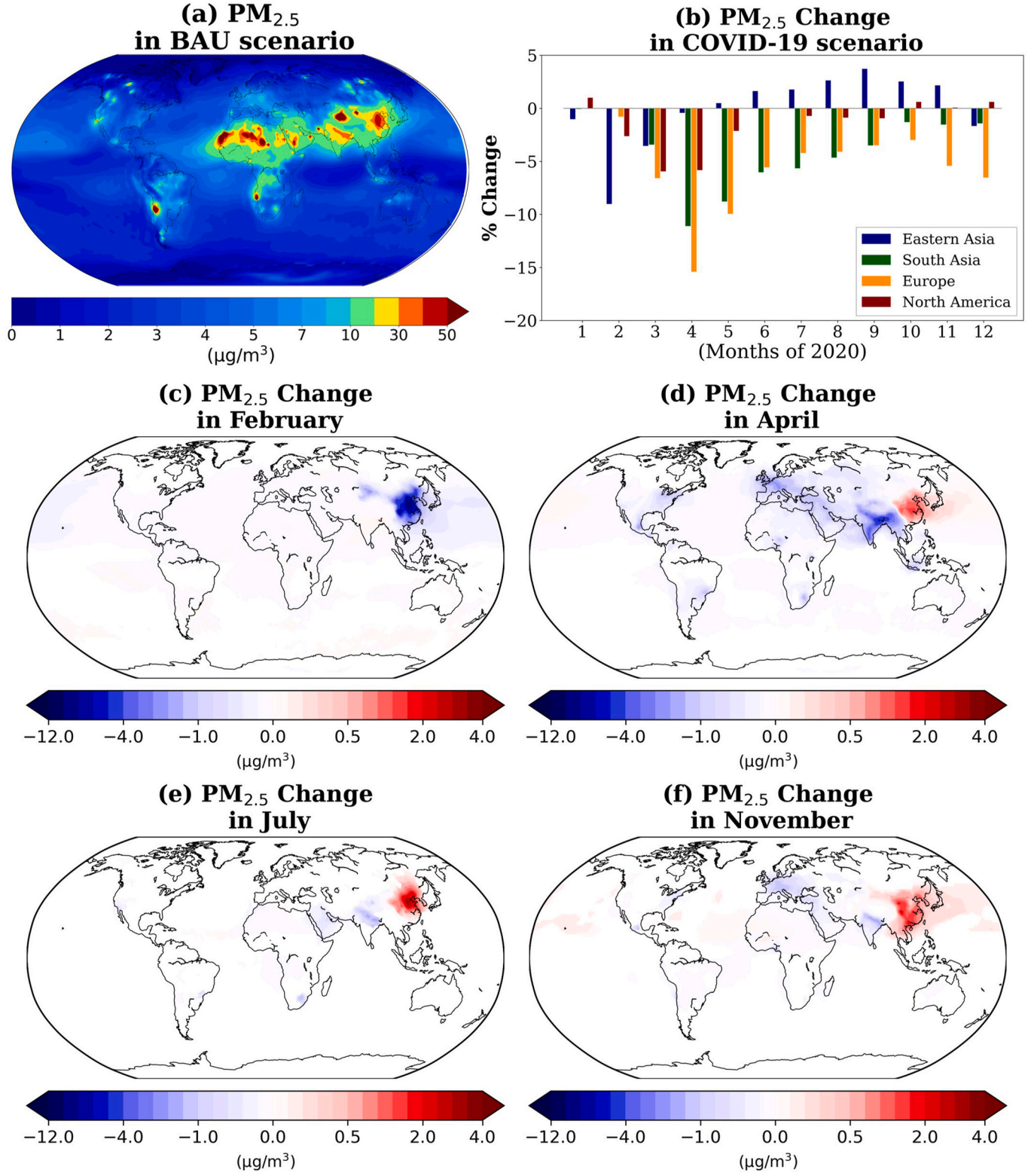

Fig. 12. **(a)** Annual average total $PM_{2.5}$ concentration (μg m^{-3}) in the BAU scenario, **(b)** monthly average $PM_{2.5}$ concentration change (%) during 2020 at specific locations and monthly average spatial $PM_{2.5}$ concentration change (μg m^{-3}) in **(c)** February, **(d)** April, **(e)** July and **(f)** November between BAU and COVID-19 and scenario; a negative change (blue) corresponds to a decrease in $PM_{2.5}$ concentration during COVID-19. (For interpretation of the references to colour in this figure legend, the reader is referred to the Web version of this article.)

oxidant levels increased (Fig. S5). In both continents, SOA reduction events became less pronounced after the summer months due to the interruption of the quarantine measures and began to occur again around November–December. In North America, the largest decrease occurred in April and May (11 % and 9 %, respectively), while the largest increase occurred in December (5 %), the month in which oxidant concentrations also increased (Fig. S5). After May, the decreasing effects were less pronounced until the increasing effect after

Table 5
Percentage monthly and annual difference (%) of total fine particulate matter concentrations between COVID-19 and BAU scenario during the year 2020. A negative result indicates a decrease during COVID-19.

	$PM_{2.5}$				
	Feb.	*Apr.*	*Jul.*	*Nov.*	*Ann.*
North America	−2.7	−5.9	−0.7	0.1	−1.4
Europe	−0.8	−15.4	−4.2	−5.5	−5.4
Eastern Asia	−9.1	−0.5	1.8	2.2	−0.1
Southern Asia	0.0	−11.1	−5.7	−1.6	−4.0
Eurasia	−1.0	−8.4	−1.1	−3.7	−2.8
South-East Asia and Developing Pacific	−1.4	−6.1	−2.6	0.7	−2.2
Asia-Pacific Developed	0.0	−1.5	−1.3	−0.4	−0.6
Middle East	−0.2	−4.2	−2.1	−1.5	−1.9
Africa	−0.1	−3.1	−1.0	−0.5	−1.0
Latin America & Caribbean	−0.2	−5.7	−3.9	−1.7	−2.6

October. In Eastern Asia the largest decrease was during February (7 %), while after May, increasing results were calculated until the end of the year (Fig. 11). The largest increase in Eastern Asia was in September (6 %). Tian et al. (2021) also reported that in China the increase in O_3 and NO_3 radicals during the lockdown promoted SOA formation. Latin America and the Caribbean also experienced significant declines, with a global annual decline of approximately 8 %. It is important to note that the model does not include emissions from cooking and volatile chemical products (VCPs) emissions. Recent studies have identified these sources as significant emerging contributors to anthropogenic VOC emissions, capable of influencing urban atmospheric chemistry (Stavroulas et al., 2019; Gkatzelis et al., 2021a; Coggon et al., 2021). Consequently, the omission of these emissions may result in underestimations of modeled SOA concentrations and could potentially impact the interpretation of pollutant responses to pandemic-related restrictions presented in this study.

5.6. Total fine particulate matter

The annual average surface concentration of $PM_{2.5}$ is reported to be 8.1 μg m^{-3} over land and 3.7 μg m^{-3} globally. Eastern and Southern Asia have the highest average annual concentrations at approximately 20 μg m^{-3}. The Middle East and Africa also have significant concentrations, averaging ~16 μg m^{-3}, particularly during the summer months (Fig. 12b, Table 5). In contrast, North America has the lowest average concentration at 2.6 μg m^{-3}, followed by Eurasia at 3.2 μg m^{-3} and the Asia-Pacific Developed region at 3.4 μg m^{-3}. After applying the CONFORM emission adjustment factors, the global annual average $PM_{2.5}$ concentrations over land decreased by 4 %. In Southern Asia, the largest monthly reduction was observed in April (11 %; Fig. 12d–Table 5). Observations from India indicate a decrease in $PM_{2.5}$ of up to 37 % (March–May 2020) compared to the period 2017–2019 (Kant et al., 2020), while additional studies report $PM_{2.5}$ declines of 10–20 % across various Indian regions (Patel et al., 2024). The simulated reductions were less pronounced after April, with the smallest calculated in October (1 %). In Europe, the largest reduction also occurred in April (15 %; Fig. 12), which is consistent with the results of Venter et al. (2020) and Evangeliou et al. (2025) and corresponds to approximately 1 μg m^{-3}, consistent with Hammer et al. (2021). The smallest decrease in Europe occurred in October (3 %), but reductions intensified after that month. In North America, the largest reduction occurred in March (6 %), with levels gradually returning to BAU levels by July (Fig. 12). In East Asia, the largest decrease in $PM_{2.5}$ occurred in February (9 %), which is lower than the 24 % decrease reported by Zheng et al. (2021) for the same period. On the other hand, September showed the largest increase (4 %; Fig. 12). Seasonal variations in Eastern Asia showed increasing concentrations from April to September, followed by a decreasing trend, culminating in a 2 % decrease in December.

6. Conclusions

This study explores the global impact of emission changes on atmospheric trace gases and aerosols during the COVID-19 pandemic. The analysis encompasses key gas pollutants (e.g., O_3, NO_x, SO_2), inorganic aerosols (sulfate, nitrate, ammonium), and organic aerosols, including primary organic aerosol (POA) and secondary organic aerosols (SOA) from the oxidation of SVOCs, IVOCs, and VOCs.

Most regions experienced declines in pollutant concentrations during lockdowns. Eastern Asia saw the steepest declines in February (except for O_3), with subsequent increases in pollutants after spring. SO_2 and sulfate aerosols registered the largest annual increases (5 % and 1.5 %, respectively), attributed mainly to industrial activity increases, as indicated by emission activity factors. Additionally, oxidants are critical to aerosol formation. Therefore, even small increases in oxidants (e.g., O_3, OH, etc.) can substantially influence aerosol concentrations, such as sulfate and SOA. Europe recorded substantial decreases in secondary pollutants, especially in April, though O_3 saw only a modest annual average decrease of 0.3 %, due to rising levels in November and December. $PM_{2.5}$ (5.5 %) and nitrate aerosols (9.4 %) showed the largest continental reductions with significant seasonal variability. Pollutant declines were less pronounced in summer, with a marked rebound in the autumn, reflecting adjustments in emission factors. Southern Asia, unlike Europe, did not experience a significant drop in restrictions during the summer or a second wave in the autumn. After April, when reductions peaked, declines gradually began to fade, with November and December seeing increases in NO_x and sulfate aerosols due to higher energy demands. Notably, POA and SOA from anthropogenic S/IVOC emissions saw the greatest annual decreases in Southern Asia (8.3 % and 6.4 %, respectively). North America experienced similar patterns, with notable decreases in April, moderation in summer, and a return to higher reductions by autumn. However, increases in December were evident for O_3 (0.8 %), sulfate aerosols (7.4 %), and SOA from anthropogenic S/IVOC (3.6 %) and VOC (5 %). Latin America and the Caribbean and the Middle East exhibited significant, mostly declining trends. Latin America and the Caribbean recorded the largest annual decreases for O_3 (1.4 %), NO_x (10.3 %), and SOA (7.7 %), while the Middle East registered the highest decrease in O_3 (1.4 %).

In conclusion, this study highlights the complex and regionally diverse responses of atmospheric trace gases and aerosols to changes in emissions during the COVID-19 pandemic. The results reveal the interaction between emission reductions and atmospheric chemistry, providing important insights into the dynamics of air pollution in unprecedented situations. While the noticeable decreases in pollutants during lockdowns illustrate the potential of emission reductions to improve air quality, the subsequent rebound and regional differences emphasize the temporary nature of these changes. These findings highlight the importance of implementing sustained, systemic measures to achieve lasting improvements in air quality.

CRediT authorship contribution statement

Apostolos T. Koumparos: Writing – original draft, Formal analysis. **Vlassis A. Karydis:** Writing – review & editing, Methodology, Investigation. **Georgios I. Gkatzelis:** Writing – review & editing, Validation. **Nikolaos Mihalopoulos:** Writing – review & editing, Validation. **Alexandra P. Tsimpidi:** Writing – review & editing, Validation, Supervision, Methodology, Investigation, Conceptualization.

Code and data availability

The usage of MESSy (Modular Earth Submodel System) and access to the source code is licensed to all affiliates of institutions which are members of the MESSy Consortium. Institutions can become a member of the MESSy Consortium by signing the "MESSy Memorandum of Understanding". More information can be found on the MESSy Consortium

website: http://www.messy-interface.org (last access: February 24, 2025). CAMS v4.2 anthropogenic emissions inventory was obtained from https://eccad.sedoo.fr/#/catalogue (last access: February 24, 2025). CONFORM adjustment factors data were downloaded from https://eccad.aeris-data.fr/essd-conform/(last access: February 24, 2025). The data produced in the study is available in the open access repository zenodo: https://doi.org/10.5281/zenodo.14916461 (last access: February 24, 2025).

Declaration of generative AI and AI-assisted technologies in the writing process

During the preparation of this work the author used DeepL Write in order to improve language and readability. After using this tool, the authors reviewed and edited the content as needed and take full responsibility for the content of the publication.

Declaration of competing interest

The authors declare that they have no known competing financial interests or personal relationships that could have appeared to influence the work reported in this paper.

Acknowledgments

The authors gratefully acknowledge the Earth System Modelling Project (ESM) for funding this work by providing computing time on the ESM partition of the supercomputer JUWELS (Alvarez, 2021) at the Jülich Supercomputing Centre (JSC).

Appendix A. Supplementary data

Supplementary data to this article can be found online at https://doi.org/10.1016/j.aeaoa.2025.100361.

References

Adam, M.G., Tran, P.T.M., Balasubramanian, R., 2021. Air quality changes in cities during the COVID-19 lockdown: a critical review. Atmos. Res. 264, 105823. https://doi.org/10.1016/j.atmosres.2021.105823.

Alvarez, D., 2021. JUWELS cluster and booster: exascale pathfinder with modular supercomputing architecture at juelich supercomputing centre. J. Large-scale Res. Facilities JLSRF 7. https://doi.org/10.17815/jlsrf-7-183.

Amritha, S., Patel, V.K., Kuttippurath, J., Hamza, V., 2024. The COVID-19 lockdown induced changes of SO2 pollution in its Human-made global hotspots. Glob Transit 6, 152–163. https://doi.org/10.1016/j.glt.2024.06.003.

Bouarar, I., Gaubert, B., Brasseur, G.P., Steinbrecht, W., Doumbia, T., Tilmes, S., Liu, Y. M., Stavrakou, T., Deroubaix, A., Darras, S., Granier, C., Lacey, F., Müller, J.F., Shi, X.Q., Elguindi, N., Wang, T., 2021. Ozone anomalies in the free troposphere during the COVID-19 pandemic. Geophys. Res. Lett. 48, e2021GL094204. https://doi.org/10.1029/2021GL094204.

Bouwman, A.F., Lee, D.S., Asman, W.A.H., Dentener, F.J., VanderHoek, K.W., Olivier, J. G.J., 1997. A global high-resolution emission inventory for ammonia. Glob. Biogeochem. Cycles 11, 561–587. https://doi.org/10.1029/97gb02266.

Camargo-Caicedo, Y., Mantilla-Romo, L.C., Bolaño-Ortiz, T.R., 2021. Emissions reduction of greenhouse gases, ozone precursors, aerosols and acidifying gases from road transportation during the COVID-19 lockdown in Colombia. Appl Sci-Basel 11, 1458. https://doi.org/10.3390/app11041458.

Cameletti, M., 1994. The effect of Corona virus lockdown on air pollution: evidence from the city of brescia in lombardia region (italy). Atmos. Environ. 239, 117794. https://doi.org/10.1016/j.atmosenv.2020.117794, 2020.

Campbell, P.C., Tong, D., Tang, Y., Baker, B., Lee, P., Saylor, R., Stein, A., Ma, S., Lamsal, L., Qu, Z., 1994. Impacts of the COVID-19 economic slowdown on ozone pollution in the U.S. Atmos. Environ. 264, 118713. https://doi.org/10.1016/j.atmosenv.2021.118713, 2021.

Cao, Y., Shao, L., Jones, T., Oliveira, M.L.S., Ge, S., Feng, X., Silva, L.F.O., BeruBe, K., 2021. Multiple relationships between aerosol and COVID-19: a framework for global studies. Gondwana Res. 93, 243–251. https://doi.org/10.1016/j.gr.2021.02.002.

Casallas, A., Cabrera, A., Guevara-Luna, M.A., Tompkins, A., Gonzalez, Y., Aranda, J., Belalcazar, L.C., Mogollon-Sotelo, C., Celis, N., Lopez-Barrera, E., Pena-Rincon, C.A., Ferro, C., 2024. Air pollution analysis in northwestern South America: a new Lagrangian framework. Sci. Total Environ. 906, 167350. https://doi.org/10.1016/j.scitotenv.2023.167350.

Coggon, M.M., Gkatzelis, G.I., McDonald, B.C., Gilman, J.B., Schwantes, R.H., Abuhassan, N., Aikin, K.C., Arend, M.F., Berkoff, T.A., Brown, S.S., Campos, T.L., Dickerson, R.R., Gronoff, G., Hurley, J.F., Isaacman-VanWertz, G., Koss, A.R., Li, M., McKeen, S.A., Moshary, F., Peischl, J., Pospisilova, V., Ren, X.R., Wilson, A., Wu, Y. H., Trainer, M., Warneke, C., 2021. Volatile chemical product emissions enhance ozone and modulate urban chemistry. Proc. Natl. Acad. Sci. U. S. A 118. https://doi.org/10.1073/pnas.2026653118.

Collivignarelli, M.C., Abba, A., Bertanza, G., Pedrazzani, R., Ricciardi, P., Carnevale Miino, M., 2020. Lockdown for CoViD-2019 in milan: what are the effects on air quality? Sci. Total Environ. 732, 139280. https://doi.org/10.1016/j.scitotenv.2020.139280.

Cuesta, J., Costantino, L., Beekmann, M., Siour, G., Menut, L., Bessagnet, B., Landi, T.C., Dufour, G., Eremenko, M., 2022. Ozone pollution during the COVID-19 lockdown in the spring of 2020 over Europe, analysed from satellite observations, in situ measurements, and models. Atmos. Chem. Phys. 22, 4471–4489. https://doi.org/10.5194/acp-22-4471-2022.

Dentener, F., Kinne, S., Bond, T., Boucher, O., Cofala, J., Generoso, S., Ginoux, P., Gong, S., Hoelzemann, J.J., Ito, A., Marelli, L., Penner, J.E., Putaud, J.P., Textor, C., Schulz, M., van der Werf, G.R., Wilson, J., 2006. Emissions of primary aerosol and precursor gases in the years 2000 and 1750 prescribed data-sets for AeroCom. Atmos. Chem. Phys. 6, 4321–4344. https://doi.org/10.5194/acp-6-4321-2006.

Deroubaix, A., Brasseur, G., Gaubert, B., Labuhn, I., Menut, L., Siour, G., Tuccella, P., 2021. Response of surface ozone concentration to emission reduction and meteorology during the COVID-19 lockdown in Europe. Meteorol. Appl. 28. https://doi.org/10.1002/met.1990.

Dong, X., Zheng, X., Wang, C., Zeng, J., Zhang, L., 2022. Air pollution rebound and different recovery modes during the period of easing COVID-19 restrictions. Sci. Total Environ. 843, 156942. https://doi.org/10.1016/j.scitotenv.2022.156942.

Doumbia, T., Granier, C., Elguindi, N., Bouarar, I., Darras, S., Brasseur, G., Gaubert, B., Liu, Y.M., Shi, X.Q., Stavrakou, T., Tilmes, S., Lacey, F., Deroubaix, A., Wang, T., 2021. Changes in global air pollutant emissions during the COVID-19 pandemic: a dataset for atmospheric modeling. Earth Syst. Sci. Data 13, 4191–4206. https://doi.org/10.5194/essd-13-4191-2021.

Evangeliou, N., Tichý, O., Svendby Otervik, M., Eckhardt, S., Balkanski, Y., Hauglustaine, D.A., 2025. Unchanged PM2.5 levels over Europe during COVID-19 were buffered by ammonia. Aerosol Research 3, 155–174. https://doi.org/10.5194/ar-3-155-2025.

Forster, P.M., Forster, H.I., Evans, M.J., Gidden, M.J., Jones, C.D., Keller, C.A., Lamboll, R.D., Quere, C.L., Rogelj, J., Rosen, D., Schleussner, C.F., Richardson, T.B., Smith, C.J., Turnock, S.T., 2020. Erratum: publisher correction: current and future global climate impacts resulting from COVID-19. Nat. Clim. Change 10, 971. https://doi.org/10.1038/s41558-020-0904-z.

Fountoukis, C., Nenes, A., 2007. Isorropia II: a computationally efficient thermodynamic equilibrium model for K+ – Ca2+ – Mg2+ – NH4+ – Na+ – SO(4)(2-) – NO3- – Cl- – H2O aerosols. Atmos. Chem. Phys. 7, 4639–4659. https://doi.org/10.5194/acp-7-4639-2007.

Fu, F., Purvis-Roberts, K.L., Williams, B., 2020. Impact of the COVID-19 pandemic lockdown on air pollution in 20 major cities around the world. Atmosphere-Basel 11. https://doi.org/10.3390/atmos11111189.

Gao, C., Li, S., Liu, M., Zhang, F., Achal, V., Tu, Y., Zhang, S., Cai, C., 2021. Impact of the COVID-19 pandemic on air pollution in Chinese megacities from the perspective of traffic volume and meteorological factors. Sci. Total Environ. 773, 145545. https://doi.org/10.1016/j.scitotenv.2021.145545.

Gaubert, B., Bouarar, I., Doumbia, T., Liu, Y., Stavrakou, T., Deroubaix, A., Darras, S., Elguindi, N., Granier, C., Lacey, F., Muller, J.F., Shi, X., Tilmes, S., Wang, T., Brasseur, G.P., 2021. Global changes in secondary atmospheric pollutants during the 2020 COVID-19 pandemic. J. Geophys. Res. Atmos. 126, e2020JD034213. https://doi.org/10.1029/2020JD034213.

Giani, P., Castruccio, S., Anav, A., Howard, D., Hu, W., Crippa, P., 2020. Short-term and long-term health impacts of air pollution reductions from COVID-19 lockdowns in China and Europe: a modelling study. Lancet Planet. Health 4, e474–e482. https://doi.org/10.1016/S2542-5196(20)30224-2.

Gkatzelis, G.I., Coggon, M.M., McDonald, B.C., Peischl, J., Aikin, K.C., Gilman, J.B., Trainer, M., Warneke, C., 2021a. Identifying volatile chemical product tracer compounds in US cities. Environ. Sci. Technol. 55, 188–199. https://doi.org/10.1021/acs.est.0c05467.

Gkatzelis, G.I., Gilman, J.B., Brown, S.S., Eskes, H., Gomes, A.R., Lange, A.C., McDonald, B.C., Peischl, J., Petzold, A., Thompson, C.R., Kiendler-Scharr, A., 2021b. The global impacts of COVID-19 lockdowns on urban air pollution: a critical review and recommendations. Elementa-Sci Anthrop 9. https://doi.org/10.1525/elementa.2021.00176.

Goldberg, D.L., Anenberg, S.C., Griffin, D., McLinden, C.A., Lu, Z., Streets, D.G., 2020. Disentangling the impact of the COVID-19 lockdowns on urban NO(2) from natural variability. Geophys. Res. Lett. 47, e2020GL089269. https://doi.org/10.1029/2020GL089269.

Gopikrishnan, G.S., Kuttippurath, J., Raj, S., Singh, A., Abbhishek, K., 2022. Air quality during the COVID-19 lockdown and unlock periods in India analyzed using satellite and ground-based measurements. Environ Process 9, ARTN 28. https://doi.org/10.1007/s40710-022-00585-9.

Granier, C., Darras, S., Gon, H.D.v. d., Doubalova, J., Elguindi, N.B., Galle, M.G., Guevara, M., Jalkanen, J.-P., Kuenen, J., Liousse, C., Quack, B., Simpson, D., Sindelarova, K., 2019. The copernicus atmosphere monitoring service global and regional emissions (april 2019 version). https://doi.org/10.24380/eets-qd81.

Grewe, V., Brunner, D., Dameris, M., Grenfell, J.L., Hein, R., Shindell, D., Staehelin, J., 2001. Origin and variability of upper tropospheric nitrogen oxides and ozone at northern mid-latitudes. Atmos. Environ. 35, 3421–3433. https://doi.org/10.1016/S1352-2310(01)00134-0, 10.1016/s1352-2310(01)00134-0.

Guevara, M., Petetin, H., Jorba, O., van der Gon, H.D., Kuenen, J., Super, I., Jalkanen, J. P., Majamäki, E., Johansson, L., Peuch, V.H., García-Pando, C.P., 2022. European primary emissions of criteria pollutants and greenhouse gases in 2020 modulated by the COVID-19 pandemic disruptions. Earth Syst. Sci. Data 14, 2521–2552. https://doi.org/10.5194/essd-14-2521-2022.

Hammer, M.S., van Donkelaar, A., Martin, R.V., McDuffie, E.E., Lyapustin, A., Sayer, A. M., Hsu, N.C., Levy, R.C., Garay, M.J., Kalashnikova, O.V., Kahn, R.A., 2021. Effects of COVID-19 lockdowns on fine particulate matter concentrations. Sci. Adv. 7, 10. https://doi.org/10.1126/sciadv.abg7670.

Han, Z., Zhang, Y., Liu, Z., Zhang, K., Wang, Z., Luo, B., Xue, L., Wang, X., 2024. The Impact of COVID-19 Lockdown on Surface Air Quality Changes in Major African Countries. EGUsphere, pp. 1–29. https://doi.org/10.5194/egusphere-2024-2951, 2024.

Hanaoka, T., Masui, T., 2020. Exploring effective short-lived climate pollutant mitigation scenarios by considering synergies and trade-offs of combinations of air pollutant measures and low carbon measures towards the level of the 2 degrees C target in Asia. Environ. Pollut. 261, 113650. https://doi.org/10.1016/j.envpol.2019.113650.

Hersbach, H., Bell, B., Berrisford, P., Hirahara, S., Horányi, A., Muñoz-Sabater, J., Nicolas, J., Peubey, C., Radu, R., Schepers, D., Simmons, A., Soci, C., Abdalla, S., Abellan, X., Balsamo, G., Bechtold, P., Biavati, G., Bidlot, J., Bonavita, M., De Chiara, G., Dahlgren, P., Dee, D., Diamantakis, M., Dragani, R., Flemming, J., Forbes, R., Fuentes, M., Geer, A., Haimberger, L., Healy, S., Hogan, R.J., Hólm, E., Janisková, M., Keeley, S., Laloyaux, P., Lopez, P., Lupu, C., Radnoti, G., de Rosnay, P., Rozum, I., Vamborg, F., Villaume, S., Thépaut, J.N., 2020. The ERA5 global reanalysis. Q. J. Roy. Meteorol. Soc. 146, 1999–2049. https://doi.org/10.1002/qj.3803.

Huang, X., Ding, A., Gao, J., Zheng, B., Zhou, D., Qi, X., Tang, R., Wang, J., Ren, C., Nie, W., Chi, X., Xu, Z., Chen, L., Li, Y., Che, F., Pang, N., Wang, H., Tong, D., Qin, W., Cheng, W., Liu, W., Fu, Q., Liu, B., Chai, F., Davis, S.J., Zhang, Q., He, K., 2021. Enhanced secondary pollution offset reduction of primary emissions during COVID-19 lockdown in China. Natl. Sci. Rev. 8, nwaa137. https://doi.org/10.1093/nsr/nwaa137.

Jaffe, D., Anderson, T., Covert, D., Kotchenruther, R., Trost, B., Danielson, J., Simpson, W., Berntsen, T., Karlsdottir, S., Blake, D., Harris, J., Carmichael, G., Uno, I., 1999. Transport of Asian air pollution to North America. Geophys. Res. Lett. 26, 711–714. https://doi.org/10.1029/1999gl900100.

Jia, C.R., Fu, X.Q., Bartelli, D., Smith, L., 2020. Insignificant impact of the "stay-at-home" order on ambient air quality in the Memphis metropolitan area, USA. Atmosphere-Basel 11. https://doi.org/10.3390/atmos11060630.

Jöckel, P., Sander, R., Kerkweg, A., Tost, H., Lelieveld, J., 2005. Technical note:: the modular Earth submodel system (MESSy) -: a new approach towards Earth system modeling. Atmos. Chem. Phys. 5, 433–444. https://doi.org/10.5194/acp-5-433-2005.

Karydis, V.A., Capps, S.L., Russell, A.G., Nenes, A., 2012. Adjoint sensitivity of global cloud droplet number to aerosol and dynamical parameters. Atmos. Chem. Phys. 12, 9041–9055. https://doi.org/10.5194/acp-12-9041-2012.

Karydis, V.A., Tsimpidi, A.P., Pozzer, A., Astitha, M., Lelieveld, J., 2016. Effects of mineral dust on global atmospheric nitrate concentrations. Atmos. Chem. Phys. 16, 1491–1509. https://doi.org/10.5194/acp-16-1491-2016.

Karydis, V.A., Tsimpidi, A.P., Bacer, S., Pozzer, A., Nenes, A., Lelieveld, J., 2017. Global impact of mineral dust on cloud droplet number concentration. Atmos. Chem. Phys. 17, 5601–5621. https://doi.org/10.5194/acp-17-5601-2017.

Karydis, V.A., Tsimpidi, A.P., Pozzer, A., Lelieveld, J., 2021. How alkaline compounds control atmospheric aerosol particle acidity. Atmos. Chem. Phys. 21, 14983–15001. https://doi.org/10.5194/acp-21-14983-2021.

Keller, C.A., Evans, M.J., Knowland, K.E., Hasenkopf, C.A., Modekurty, S., Lucchesi, R.A., Oda, T., Franca, B.B., Mandarino, F.C., Suarez, M.V.D., Ryan, R.G., Fakes, L.H., Pawson, S., 2021. Global impact of COVID-19 restrictions on the surface concentrations of nitrogen dioxide and ozone. Atmos. Chem. Phys. 21, 3555–3592. https://doi.org/10.5194/acp-21-3555-2021.

Klingmuller, K., Metzger, S., Abdelkader, M., Karydis, V.A., Stenchikov, G.L., Pozzer, A., Lelieveld, J., 2018. Revised mineral dust emissions in the atmospheric chemistry-climate model EMAC (MESSy 2.52 DU_Astitha1 KKDU2017 patch). Geosci. Model Dev. (GMD) 11, 989–1008. https://doi.org/10.5194/gmd-11-989-2018.

Kong, L., Tang, X., Zhu, J., Wang, Z.F., Sun, Y.L., Fu, P.Q., Gao, M., Wu, H.J., Lu, M.M., Wu, Q., Huang, S.Y., Sui, W.X., Li, J., Pan, X.L., Wu, L., Akimoto, H., Carmichael, G. R., 2023. Unbalanced emission reductions of different species and sectors in chinaduring COVID-19 lockdown derived by multi-species surface observationassimilation. Atmos. Chem. Phys. 23, 6217–6240. https://doi.org/10.5194/acp-23-6217-2023, 10.5194/acp-5-433-2005.

Kutralam-Muniasamy, G., Perez-Guevara, F., Roy, P.D., Elizalde-Martinez, I., Shruti, V. C., 2021. Impacts of the COVID-19 lockdown on air quality and its association with human mortality trends in megapolis Mexico City. Air Qual. Atmos. Health 14, 553–562. https://doi.org/10.5194/acp-5-433-200510.1007/s11869-020-00960-1.

Kuttippurath, J., Patel, V.K., Kashyap, R., Singh, A., Clerbaux, C., 2024. Anomalous increase in global atmospheric ammonia during COVID-19 lockdown: need policies to curb agricultural emissions. J. Clean. Prod. 434. https://doi.org/10.5194/acp-5-433-200510.1016/j.jclepro.2023.140424.

Le, T., Wang, Y., Liu, L., Yang, J., Yung, Y.L., Li, G., Seinfeld, J.H., 2020. Unexpected air pollution with marked emission reductions during the COVID-19 outbreak in China. Science 369, 702–706. https://doi.org/10.1126/science.abb7431.

Li, Z., Yu, S., Li, M., Chen, X., Zhang, Y., Li, J., Jiang, Y., Liu, W., Li, P., Lichtfouse, E., 2022. Non-stop industries were the main source of air pollution during the 2020 coronavirus lockdown in the north China plain. Environ. Chem. Lett. 20, 59–69. https://doi.org/10.1007/s10311-021-01314-8.

Lian, X., Huang, J., Huang, R., Liu, C., Wang, L., Zhang, T., 2020. Impact of city lockdown on the air quality of COVID-19-hit of wuhan city. Sci. Total Environ. 742, 140556. https://doi.org/10.1016/j.scitotenv.2020.140556.

Lin, J., Pan, D., Davis, S.J., Zhang, Q., He, K., Wang, C., Streets, D.G., Wuebbles, D.J., Guan, D., 2014. China's international trade and air pollution in the United States. Proc. Natl. Acad. Sci. U. S. A. 111, 1736–1741. https://doi.org/10.1073/pnas.1312860111.

Liu, F., Wang, M., Zheng, M., 2021a. Effects of COVID-19 lockdown on global air quality and health. Sci. Total Environ. 755, 142533. https://doi.org/10.1016/j.scitotenv.2020.142533.

Liu, L., Zhang, J., Du, R., Teng, X., Hu, R., Yuan, Q., Tang, S., Ren, C., Huang, X., Xu, L., Zhang, Y., Zhang, X., Song, C., Liu, B., Lu, G., Shi, Z., Li, W., 2021b. Chemistry of atmospheric fine particles during the COVID-19 pandemic in a megacity of eastern China. Geophys. Res. Lett. 48, 2020GL091611. https://doi.org/10.1029/2020GL091611.

Liu, Z., Ciais, P., Deng, Z., Lei, R., Davis, S.J., Feng, S., Zheng, B., Cui, D., Dou, X., Zhu, B., Guo, R., Ke, P., Sun, T., Lu, C., He, P., Wang, Y., Yue, X., Wang, Y., Lei, Y., Zhou, H., Cai, Z., Wu, Y., Guo, R., Han, T., Xue, J., Boucher, O., Boucher, E., Chevallier, F., Tanaka, K., Wei, Y., Zhong, H., Kang, C., Zhang, N., Chen, B., Xi, F., Liu, M., Breon, F. M., Lu, Y., Zhang, Q., Guan, D., Gong, P., Kammen, D.M., He, K., Schellnhuber, H.J., 2020. Near-real-time monitoring of global CO(2) emissions reveals the effects of the COVID-19 pandemic. Nat. Commun. 11, 5172. https://doi.org/10.1038/s41467-020-20254-5.

Lu, Z., Wang, J., Wang, Y., Henze, D.K., Chen, X., Sha, T., Sun, K., 2024. Aggravated surface O3 pollution primarily driven by meteorological variations in China during the 2020 COVID-19 pandemic lockdown period. Atmos. Chem. Phys. 24, 7793–7813. https://doi.org/10.5194/acp-24-7793-2024.

Milousis, A., Tsimpidi, A.P., Tost, H., Pandis, S.N., Nenes, A., Kiendler-Scharr, A., Karydis, V.A., 2024. Implementation of the ISORROPIA-Lite aerosol thermodynamics model into the EMAC chemistry climate model (based on MESSy v2.55): implications for aerosol composition and acidity. Geosci. Model Dev. (GMD) 17, 1111–1131. https://doi.org/10.5194/gmd-17-1111-2024.

Milousis, A., Klingmüller, K., Tsimpidi, A.P., Kok, J.F., Kanakidou, M., Nenes, A., Karydis, V.A., 2025a. Impact of mineral dust on the global nitrate aerosol direct and indirect radiative effect. Atmos. Chem. Phys. 25, 1333–1351. https://doi.org/10.5194/acp-25-1333-2025.

Milousis, A., Scholz, S.M.C., Fuchs, H., Tsimpidi, A.P., Karydis, V.A., 2025. Global Perspectives on Nitrate Aerosol Dynamics: a Comprehensive Sensitivity Analysis. EGUsphere, pp. 1–42. https://doi.org/10.5194/egusphere-2025-313,202b.

Niu, H.Y., Zhang, C.C., Hu, W., Hu, T.F., Wu, C.M., Hu, S.H., Silva, L.F.O., Gao, N.N., Bao, X.L., Fan, J.S., 2022. Air quality changes during the COVID-19 lockdown in an industrial city in north China: post-pandemic proposals for air quality improvement. Sustainability-Basel 14. https://doi.org/10.3390/su141811531.

Ortega, I., Gaubert, B., Hannigan, J.W., Brasseur, G., Worden, H.M., Blumenstock, T., Fu, H., Hase, F., Jeseck, P., Jones, N., Liu, C., Mahieu, E., Morino, I., Murata, I., Notholt, J., Palm, M., Röhling, A., Té, Y., Strong, K., Sun, Y.W., Yamanouchi, S., 2023. Anomalies of O3, CO, C2H2, H2CO, and C2H6 detected with multiple ground-based Fourier-transform infrared spectrometers and assessed with model simulation in 2020: COVID-19 lockdowns versus natural variability. Elementa-Sci Anthrop 11, 12–23. https://doi.org/10.1525/elementa.2023.00015.

Pardo Amaya, D., Samuel, S., 2022. Assessment of the Impact of Vehicle Emissions on Air Quality Changes During COVID-19 Lockdown in Bogota, Colombia. SAE Technical Paper Series. https://doi.org/10.4271/2022-01-0583.

Patel, H., Talbot, N., Salmond, J., Dirks, K., Xie, S., Davy, P., 2020. Implications for air quality management of changes in air quality during lockdown in Auckland (new zealand) in response to the 2020 SARS-CoV-2 epidemic. Sci. Total Environ. 746, 141129. https://doi.org/10.1016/j.scitotenv.2020.141129.

Patel, V.K., Kuttippurath, J., Kashyap, R., 2024. Increased global cropland greening as a response to the unusual reduction in atmospheric $PM_{2.5}$ concentrations during the COVID-19 lockdown period. Chemosphere 358, 142147. https://doi.org/10.1016/j.chemosphere.2024.142147.

Petetin, H., Bowdalo, D., Soret, A., Guevara, M., Jorba, O., Serradell, K., Pérez García-Pando, C., 2020. Meteorology-normalized impact of the COVID-19 lockdown upon NO_2 pollution in Spain. Atmos. Chem. Phys. 20, 11119–11141. https://doi.org/10.5194/acp-20-11119-2020.

Pathak, M., Patel, V.K., Kuttippurath, J., 2023. Spatial heterogeneity in global atmospheric CO during the COVID-19 lockdown: implications for global and regional air quality policies. Environ. Pollut. 335, 122269. https://doi.org/10.1016/j.envpol.2023.122269.

Poullain, M., Guerrieri, J.M., Miller, M.E., Utgés, M.E., Santini, M.S., Acosta, M.M., Fernández, A., Marsico, F.L., 2022. NO2 pollution decrease in big cities of latin america during COVID-19 pandemic. medRxiv, 22277819. https://doi.org/10.1101/2022.08.08.22277819, 2022.2008.2008.

Pozzer, A., Jöckel, P.J., Sander, R., Williams, J., Ganzeveld, L., Lelieveld, J., 2006. Technical note:: the MESSy-submodel AIRSEA calculating the air-sea exchange of chemical species. Atmos. Chem. Phys. 6, 5435–5444. https://doi.org/10.5194/acp-6-5435-2006.

Pozzer, A., Reifenberg, S.F., Kumar, V., Franco, B., Kohl, M., Taraborrelli, D., Gromov, S., Ehrhart, S., Jöckel, P., Sander, R., Fall, V., Rosanka, S., Karydis, V., Akritidis, D., Emmerichs, T., Crippa, M., Guizzardi, D., Kaiser, J.W., Clarisse, L., Kiendler-Scharr, A., Tost, H., Tsimpidi, A., 2022. Simulation of organics in the atmosphere: evaluation of EMACv2.54 with the mainz organic mechanism (MOM) coupled to the ORACLE (V1.0) submodel. Geosci. Model Dev. (GMD) 15, 2673–2710. https://doi.org/10.5194/gmd-15-2673-2022.

Pringle, K.J., Tost, H., Message, S., Steil, B., Giannadaki, D., Nenes, A., Fountoukis, C., Stier, P., Vignati, E., Leieved, J., 2010. Description and evaluation of GMXe: a new

aerosol submodel for global simulations (v1). Geosci. Model Dev. (GMD) 3, 391–412. https://doi.org/10.5194/gmd-3-391-2010.
Ren, L.L., Yang, Y., Wang, H.L., Wang, P.Y., Chen, L., Zhu, J., Liao, H., 2021. Aerosol transport pathways and source attribution in China during the COVID-19 outbreak. Atmos. Chem. Phys. 21, 15431–15445. https://doi.org/10.5194/acp-21-15431-2021.
Rodriguez-Urrego, D., Rodriguez-Urrego, L., 2020. Air quality during the COVID-19: PM (2.5) analysis in the 50 Most polluted capital cities in the world. Environ. Pollut. 266, 115042. https://doi.org/10.1016/j.envpol.2020.115042.
Roeckner, E., Brokopf, R., Esch, M., Giorgetta, M., Hagemann, S., Kornblueh, L., Manzini, E., Schlese, U., Schulzweida, U., 2006. Sensitivity of simulated climate to horizontal and vertical resolution in the ECHAM5 atmosphere model. J. Clim. 19, 3771–3791. https://doi.org/10.1175/jcli3824.1.
Ropkins, K., Tate, J.E., 2021. Early observations on the impact of the COVID-19 lockdown on air quality trends across the UK. Sci. Total Environ. 754, 142374. https://doi.org/10.1016/j.scitotenv.2020.142374.
Sanap, S.D., 1994. Global and regional variations in aerosol loading during COVID-19 imposed lockdown. Atmos. Environ. 246, 118132. https://doi.org/10.1016/j.atmosenv.2020.118132, 2021.
Sekiya, T., Miyazaki, K., Eskes, H., Bowman, K., Sudo, K., Kanaya, Y., Takigawa, M., 2023. The worldwide COVID-19 lockdown impacts on global secondary inorganic aerosols and radiative budget. Sci. Adv. 9, eadh2688. https://doi.org/10.1126/sciadv.adh2688.
Sharma, S., Zhang, M., Anshika, Gao, J., Zhang, H., Kota, S.H., 2020. Effect of restricted emissions during COVID-19 on air quality in India. Sci. Total Environ. 728, 138878. https://doi.org/10.1016/j.scitotenv.2020.138878.
Sicard, P., De Marco, A., Agathokleous, E., Feng, Z., Xu, X., Paoletti, E., Rodriguez, J.J.D., Calatayud, V., 2020. Amplified ozone pollution in cities during the COVID-19 lockdown. Sci. Total Environ. 735, 139542. https://doi.org/10.1016/j.scitotenv.2020.139542.
Skiriene, A.F., Stasiskiene, Z., 2021. COVID-19 and air pollution: measuring pandemic impact to air quality in five European countries. Atmosphere-Basel 12. https://doi.org/10.3390/atmos12030290.
Smith, S.E., Ting, M.F., Wu, Y.T., Zheng, C., 2022. Beyond the lockdowns: satellite observations of aerosol optical depth through 2020, the first year of the COVID-19 pandemic. Environ. Res. Lett. 17, 9. https://doi.org/10.1088/1748-9326/ac7889.
Stavroulas, I., Bougiatioti, A., Grivas, G., Paraskevopoulou, D., Tsagkaraki, M., Zarmpas, P., Liakakou, E., Gerasopoulos, E., Mihalopoulos, N., 2019. Sources and processes that control the submicron organic aerosol composition in an urban mediterranean environment (athens): a high temporal-resolution chemical composition measurement study. Atmos. Chem. Phys. 19, 901–919. https://doi.org/10.5194/acp-19-901-2019.
Stratoulias, D., Nuthammachot, N., 2020. Air quality development during the COVID-19 pandemic over a medium-sized urban area in Thailand. Sci. Total Environ. 746, 141320. https://doi.org/10.1016/j.scitotenv.2020.141320.
Tang, R., Huang, X., Zhou, D.R., Wang, H.K., Xu, J.W., Ding, A.J., 2021. Global air quality change during the COVID-19 pandemic: regionally different ozone pollution responses COVID-19. Atmos. Oceanogr. Sci. Libr. 14. https://doi.org/10.1016/j.aosl.2020.100015.
Tian, J., Wang, Q., Zhang, Y., Yan, M., Liu, H., Zhang, N., Ran, W., Cao, J., 2021. Impacts of primary emissions and secondary aerosol formation on air pollution in an urban area of China during the COVID-19 lockdown. Environ. Int. 150, 106426. https://doi.org/10.1016/j.envint.2021.106426.
Tost, H., Jöckel, P.J., Kerkweg, A., Sander, R., Lelieveld, J., 2006. Technical note:: a new comprehensive SCAVenging submodel for global atmospheric chemistry modelling. Atmos. Chem. Phys. 6, 565–574. https://doi.org/10.5194/acp-6-565-2006.
Tsimpidi, A.P., Karydis, V.A., Pandis, S.N., Lelieveld, J., 2016. Global combustion sources of organic aerosols: model comparison with 84 AMS factor-analysis data sets. Atmos. Chem. Phys. 16, 8939–8962. https://doi.org/10.5194/acp-16-8939-2016.
Tsimpidi, A.P., Karydis, V.A., Pandis, S.N., Lelieveld, J., 2017. Global-scale combustion sources of organic aerosols: sensitivity to formation and removal mechanisms. Atmos. Chem. Phys. 17, 7345–7364. https://doi.org/10.5194/acp-17-7345-2017.
Tsimpidi, A.P., Karydis, V.A., Pozzer, A., Pandis, S.N., Lelieveld, J., 2014. ORACLE (V1.0): module to simulate the organic aerosol composition and evolution in the atmosphere. Geosci. Model Dev. (GMD) 7, 3153–3172. https://doi.org/10.5194/gmd-7-3153-2014.
Tsimpidi, A.P., Karydis, V.A., Pozzer, A., Pandis, S.N., Lelieveld, J., 2018. ORACLE 2-D (V2.0): an efficient module to compute the volatility and oxygen content of organic aerosol with a global chemistry-climate model. Geosci. Model Dev. (GMD) 11, 3369–3389. https://doi.org/10.5194/gmd-11-3369-2018.
Tsimpidi, A.P., Scholz, S.M.C., Milousis, A., Mihalopoulos, N., Karydis, V.A., 2024. Aerosol composition trends during 2000-2020. In Depth Insights from Model Predictions and Multiple Worldwide Observation Datasets. EGUsphere, pp. 1–66. https://doi.org/10.5194/egusphere-2024-3590, 2024.
Van der Werf, G.R., Randerson, J.T., Giglio, L., Collatz, G.J., Mu, M., Kasibhatla, P.S., Morton, D.C., DeFries, R.S., Jin, Y., van Leeuwen, T.T., 2010. Global fire emissions and the contribution of deforestation, savanna, forest, agricultural, and peat fires (1997–2009). Atmos. Chem. Phys. 10, 11707–11735. https://doi.org/10.5194/acp-10-11707-2010.
Venter, Z.S., Aunan, K., Chowdhury, S., Lelieveld, J., 2020. COVID-19 lockdowns cause global air pollution declines. Proc. Natl. Acad. Sci. U. S. A. 117, 18984–18990. https://doi.org/10.1073/pnas.2006853117.
Viatte, C., Guendouz, N., Dufaux, C., Hensen, A., Swart, D., Van Damme, M., Clarisse, L., Coheur, P., Clerbaux, C., 2023. Measurement report: ammonia in paris derived from ground-based open-path and satellite observations. Atmos. Chem. Phys. 23, 15253–15267. https://doi.org/10.5194/acp-23-15253-2023.
Vignati, E., Wilson, J., Stier, P., 2004. M7: an efficient size-resolved aerosol microphysics module for large-scale aerosol transport models. J. Geophys. Res. Atmos. 109. https://doi.org/10.1029/2003jd004485.
Wang, N., Xu, J., Pei, C., Tang, R., Zhou, D., Chen, Y., Li, M., Deng, X., Deng, T., Huang, X., Ding, A., 2021. Air quality during COVID-19 lockdown in the yangtze river Delta and the pearl river Delta: two different responsive mechanisms to emission reductions in China. Environ. Sci. Technol. 55, 5721–5730. https://doi.org/10.1021/acs.est.0c08383.
Wang, X., Tsimpidi, A.P., Luo, Z., Steil, B., Pozzer, A., Lelieveld, J., Karydis, V.A., 2025. The influence of ammonia emissions on the size-resolved global. Atmospheric Aerosol Composition and Acidity. EGUsphere, pp. 1–35. https://doi.org/10.5194/egusphere-2025-527, 2025.
Wang, Y., Zhang, C.C., Pennington, E.A., He, L.Y., Yang, J.N., Yu, X.Y., Liu, Y.F., Seinfeld, J.H., 2024. Short-lived air pollutants and climate forcers through the lens of the COVID-19 pandemic. Rev. Geophys. 62, e2022RG000773. https://doi.org/10.1029/2022RG000773.
Weber, J., Shin, Y.M., Staunton Sykes, J., Archer-Nicholls, S., Abraham, N.L., Archibald, A.T., 2020. Minimal climate impacts from short-lived climate forcers following emission reductions related to the COVID-19 pandemic. Geophys. Res. Lett. 47, e2020GL090326. https://doi.org/10.1029/2020GL090326.
Xia, C., Liu, C., Cai, Z., Duan, X., Hu, Q., Zhao, F., Liu, H., Ji, X., Zhang, C., Liu, Y., 2021. Improved anthropogenic SO(2) retrieval from high-spatial-resolution satellite and its application during the COVID-19 pandemic. Environ. Sci. Technol. 55, 11538–11548. https://doi.org/10.1021/acs.est.1c01970.
Yang, Y., Ren, L.L., Li, H.M., Wang, H.L., Wang, P.Y., Chen, L., Yue, X., Liao, H., 2020. Fast climate responses to aerosol emission reductions during the COVID-19 pandemic. Geophys. Res. Lett. 47. https://doi.org/10.1029/2020GL089788.
Yienger, J.J., Levy, H., 1995. Empirical-model of global soil-biogenic NOx emissions. J. Geophys. Res. Atmos. 100, 11447–11464. https://doi.org/10.1029/95jd00370.
Zhang, R.X., Zhang, Y.Z., Lin, H.P., Feng, X., Fu, T.M., Wang, Y.H., 2020. NOx emission reduction and recovery during COVID-19 in east China. Atmosphere-Basel 11, ARTN 433. https://doi.org/10.3390/atmos11040433.
Zheng, B., Geng, G., Ciais, P., Davis, S.J., Martin, R.V., Meng, J., Wu, N., Chevallier, F., Broquet, G., Boersma, F., van der, A.R., Lin, J., Guan, D., Lei, Y., He, K., Zhang, Q., 2020. Satellite-based estimates of decline and rebound in China's CO(2) emissions during COVID-19 pandemic. Sci. Adv. 6. https://doi.org/10.1126/sciadv.abd4998.
Zheng, B., Zhang, Q., Geng, G.N., Chen, C.H., Shi, Q.R., Cui, M.S., Lei, Y., He, K.B., 2021. Changes in China's anthropogenic emissions and air quality during the COVID-19 pandemic in 2020. Earth Syst. Sci. Data 13, 2895–2907. https://doi.org/10.5194/essd-13-2895-2021.